

Quantum Monte Carlo Calculations of Light Nuclei

STEVEN C. PIEPER

Physics Division

Argonne National Laboratory

Argonne, IL 60439, USA

Summary. — During the last 15 years, there has been much progress in defining the nuclear Hamiltonian and applying quantum Monte Carlo methods to the calculation of light nuclei. I describe both aspects of this work and some recent results.

1. – Introduction

The goal of *ab-initio* light-nuclei calculations is to understand nuclei as collections of nucleons interacting with realistic (bare) potentials through reliable solutions of the many-nucleon Schrödinger equation. Such calculations can study binding energies, excitation spectra, relative stability, densities, transition amplitudes, cluster-cluster overlaps, low-energy astrophysical reactions, and other aspects of nuclei. Such calculations are also essential to claims of sub-nucleonic effects, such as medium modifications of the nuclear force or nucleon form factors; if a reliable pure nucleonic degrees of freedom calculation can reproduce experiment then there is no basis for claims of seeing sub-nucleonic degrees of freedom in that experiment (beyond the obvious fact that the free-space nucleon interactions are a result of sub-nucleonic degrees of freedom).

There are two problems in microscopic few- and many-nucleon calculations: 1) determining the Hamiltonian, and 2) given H , accurately solving the Schrödinger equation

for A nucleons; I will discuss both of these in this contribution. The two-nucleon (NN) force is determined by fitting the large body of NN scattering data. Several modern NN potentials are in common use. The Argonne v_{18} is a local potential written in operator format; this potential is used in the calculations described here, and is presented in some detail below. Other modern potentials are generally non-local; some of them are discussed in other contributions to this school.

It has long been known that calculations with just realistic NN potentials fail to reproduce the binding energies of nuclei; three-nucleon (NNN) potentials are also required. These arise naturally from an underlying meson-exchange picture of the nuclear forces or from chiral effective field theories. Unfortunately, much NNN scattering data is well reproduced by calculations using just NN forces, so the NNN force must be determined from properties of light nuclei. In this contribution the recent Illinois models with 2π and 3π rings are used.

Our understanding of nuclear forces has evolved over the last 70 years:

- Meson-exchange theory of Yukawa (1935)
- Fujita-Miyazawa three-nucleon potential (1955)
- First phase-shift analysis of NN scattering data (1957)
- Gammel-Thaler, Hamada-Johnston and Reid phenomenological potentials (1957–1968)
- Bonn, Nijmegen and Paris field-theoretic models (1970s)
- Tucson-Melbourne and Urbana NNN potential models (late 70’s–early 80’s)
- Nijmegen partial wave analysis (PWA93) with $\chi^2/\text{dof} \sim 1$ (1993)
- Nijm I, Nijm II, Reid93, Argonne v_{18} and CD-Bonn (1990s)
- Effective field theory at $N^3\text{LO}$ (2004)

References for a number of these developments are given in the following sections.

Accurate solutions of the many-nucleon Schrödinger equation have also evolved over many decades:

- ^2H by numerical integration (1952) – a pair of coupled second-order differential equations in 1 variable. At the time this took “between 5 and 20 minutes for the calculation and the printout another 5 minutes” [1]!
- ^3H by Faddeev (1975–1985)
- ^4He by Green’s function Monte Carlo (GFMC) (1988)
- $A = 6$ by GFMC and No-core shell model (NCSM) (1994-95)
- $A = 7$ by GFMC and NCSM (1997-98)
- $A = 8$ by GFMC and NCSM (2000)
- ^4He benchmark by 7 methods to 0.1% (2001)
- $A = 9, 10$ by GFMC and NCSM (2002)
- ^{12}C by GFMC and NCSM (2004–)
- ^{16}O by Coupled Cluster (CC) (2005–)

References for the $A=3,4$ calculations may be found in Ref. [2]; the GFMC calculations are the subject of this paper; the NCSM are discussed in Petr Navrátil's contribution to this Course; and CC results may be found in Ref. [3].

This contribution is limited to Variational Monte Carlo (VMC) and GFMC calculations of light nuclei. Section 2 describes the Hamiltonians used and sections 3 through 5 describe the computation methods. Section 6 gives a number of results for energies of nuclear states; Sec. 7 describes GFMC calculations of scattering states; and Sec. 8 gives some results for densities. Finally some conclusions and prospects for the future are presented in Sec. 9.

2. – Hamiltonians

The nuclear Hamiltonian used here has the form

$$(1) \quad H = \sum_i K_i + \sum_{i<j} v_{ij} + \sum_{i<j<k} V_{ijk} .$$

Here K_i is the non-relativistic kinetic energy, including $m_n - m_p$ effects, v_{ij} is the NN potential and V_{ijk} is the NNN potential.

2.1. Argonne v_{ij} . – The NN potential (v_{ij}) is Argonne v18 [4] (AV18) which has the form

$$(2) \quad v_{ij} = v_{ij}^\gamma + v_{ij}^\pi + v_{ij}^R + v_{ij}^{CIB} .$$

The v_{ij}^γ is a very complete representation of the pp , pn and nn electromagnetic terms, including first- and second-order Coulomb, magnetic, vacuum polarization, etc., components with form factors. (Ref. [5] provides a heuristic introduction to AV18.)

The v_{ij}^π is the isoscalar one-pion exchange potential represented as a local operator:

$$(3) \quad v_{ij}^\pi = \frac{1}{3} \frac{f_\pi^2}{4\pi} m_\pi X_{ij} \tau_i \cdot \tau_j ,$$

$$(4) \quad X_{ij} = T(m_\pi r_{ij}) S_{ij} + Y(m_\pi r_{ij}) \boldsymbol{\sigma}_i \cdot \boldsymbol{\sigma}_j ,$$

$$(5) \quad Y(x) = \frac{e^{-x}}{x} \xi(r) ,$$

$$(6) \quad T(x) = \left(\frac{3}{x^2} + \frac{3}{x} + 1 \right) Y(x) \xi(r) ,$$

$$(7) \quad \xi(r) = (1 - e^{-c_\pi r^2}) .$$

where τ_i , $\boldsymbol{\sigma}_i$ and S_{ij} are isospin, spin and tensor operators, respectively. In light nuclei, $\langle v_{ij}^\pi \rangle$ contributes $\sim 85\%$ of $\langle v_{ij} \rangle$.

The remaining isospin-conserving terms are

$$(8) \quad v_{ij}^R = \sum_{p=1,14} v_p(r_{ij}) O_{ij}^p ,$$

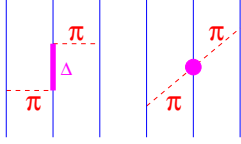


Fig. 1. – Two-pion exchange terms in the Illinois NNN potentials.

$$(9) \quad O_{ij}^{p=1,14} = [1, \sigma_i \cdot \sigma_j, S_{ij}, \mathbf{L} \cdot \mathbf{S}, \mathbf{L}^2, \mathbf{L}^2 \sigma_i \cdot \sigma_j, (\mathbf{L} \cdot \mathbf{S})^2] \otimes [1, \tau_i \cdot \tau_j],$$

where $v_p(r)$ has short-, intermediate-, and long-range components. The long-range components are just the $Y(r)$ and $T(r)$ of the one-pion potential and are present only for those operators that have contributions from one-pion exchange. The intermediate-range components are proportional to $T^2(r)$ and the short-range component is of the Woods-Saxon form.

Finally, v_{ij}^{CIB} is the strong charge independence breaking part of the potential and consists of four operators:

$$(10) \quad O_{ij}^{p=15,18} = [1, (\sigma_i \cdot \sigma_j), S_{ij}] \otimes T_{ij}, (\tau_{zi} + \tau_{zj}).$$

The long-range part of $O^{p=15,17}$ comes from one-pion exchange by inserting $m_{\pi^{+-}}$ or m_{π^0} in Eqn. (3 and 4) and using $f_{\pi NN}^2 \propto m_\pi$.

The parameters in the short- and intermediate-range components were determined by making a direct fit to the 1993 Nijmegen data base [6, 7] containing 1787 pp and 2514 np data in the range 0 – 350 MeV, the nn scattering length, and deuteron binding energy. The fit of approximately 40 parameters results in a $\chi^2/\text{d.o.f.}$ of 1.09, which is typical of 1990's NN potentials.

2.2. Illinois V_{ijk} . – The three-nucleon potential used for most of the examples presented here is the Illinois-2 [8]. It consists of two- and three-pion terms and a simple phenomenological repulsive term:

$$(11) \quad V_{ijk} = V_{ijk}^{2\pi} + V_{ijk}^{3\pi} + V_{ijk}^R.$$

The two-pion term, illustrated in Fig. 1, contains P - and S -wave πN -scattering terms:

$$(12) \quad V_{ijk}^{2\pi} = V_{ijk}^{2\pi,P} + V_{ijk}^{2\pi,S}.$$

The P -wave term (left panel of Fig. 1) is the well-known Fujita-Miyazawa [9, 10] term which is present in all realistic NNN potentials. It has the form

$$(13) \quad V_{ijk}^{2\pi,P} = A_{2\pi,P} \sum_{cyclic} \{X_{ij}, X_{jk}\} \{\tau_i \cdot \tau_j, \tau_j \cdot \tau_k\} + \frac{1}{4} [X_{ij}, X_{jk}] [\tau_i \cdot \tau_j, \tau_j \cdot \tau_k],$$

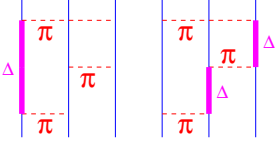


Fig. 2. – Three-pion ring terms in the Illinois NNN potentials.

where X_{ij} is defined in Eq. (4). This is the longest-ranged nuclear NNN potential and is attractive in all nuclei and nuclear matter. However it is very small or even slightly repulsive in pure neutron systems.

The second panel of Fig. 1 represents the S -wave part of $V_{ijk}^{2\pi}$. This term was introduced in the Tuscon-Melbourne NNN potential [11] and is required by chiral perturbation theory. However, in practice it is only 3%–4% of $V_{ijk}^{2\pi,P}$ in light nuclei.

The three-pion term (Fig. 2) was introduced in the Illinois potentials. It consists of the subset of three-pion rings that contain only one Δ mass in the energy denominators. Even so it has a quite complicated form which is given in Ref. [8]. An important aspect of this structure is that there is a significant attractive term which acts only in $T=3/2$ triples. In most light nuclei $\langle V_{ijk}^{3\pi} \rangle \lesssim 0.1 \langle V_{ijk}^{2\pi} \rangle$

The final term in the NNN potential, V_{ijk}^R , represents all other diagrams including relativistic effects. It is strictly phenomenological and purely central and repulsive:

$$(14) \quad V_{ijk}^R = A_R \sum_{cyclic} T^2(m_\pi r_{ij}) T^2(m_\pi r_{jk}) .$$

This repulsive term is principally needed to make nuclear matter saturate at the proper density instead of a too-high density and to obtain a hard enough equation of state for neutron matter.

The coupling constants $A_{2\pi,P}$, $A_{3\pi}$, and A_R were adjusted to fit 17 nuclear levels for $A \leq 8$. The $V_{ijk}^{2\pi,S}$ is too weak to be determined by fitting and its coupling was left at the value predicted by chiral perturbation theory.

In light nuclei we find

$$(15) \quad \langle V_{ijk} \rangle \sim (0.02 \text{ to } 0.09) \langle v_{ij} \rangle \sim (0.15 \text{ to } 0.6) \langle H \rangle$$

where the large fraction of $\langle H \rangle$ is due to a large cancellation of K and v_{ij} . From this we expect

$$(16) \quad \langle V_{4N} \rangle \sim 0.06 \langle V_{ijk} \rangle \sim (0.02 \text{ to } 0.04) \langle H \rangle \sim (0.5 \text{ to } 2.) \text{ MeV} .$$

This is comparable to the accuracy of our calculations. Even if more accurate calculations could be made, it would probably not be possible to disentangle four-nucleon potential effects from uncertainties in the fitted parameters of V_{ijk} .

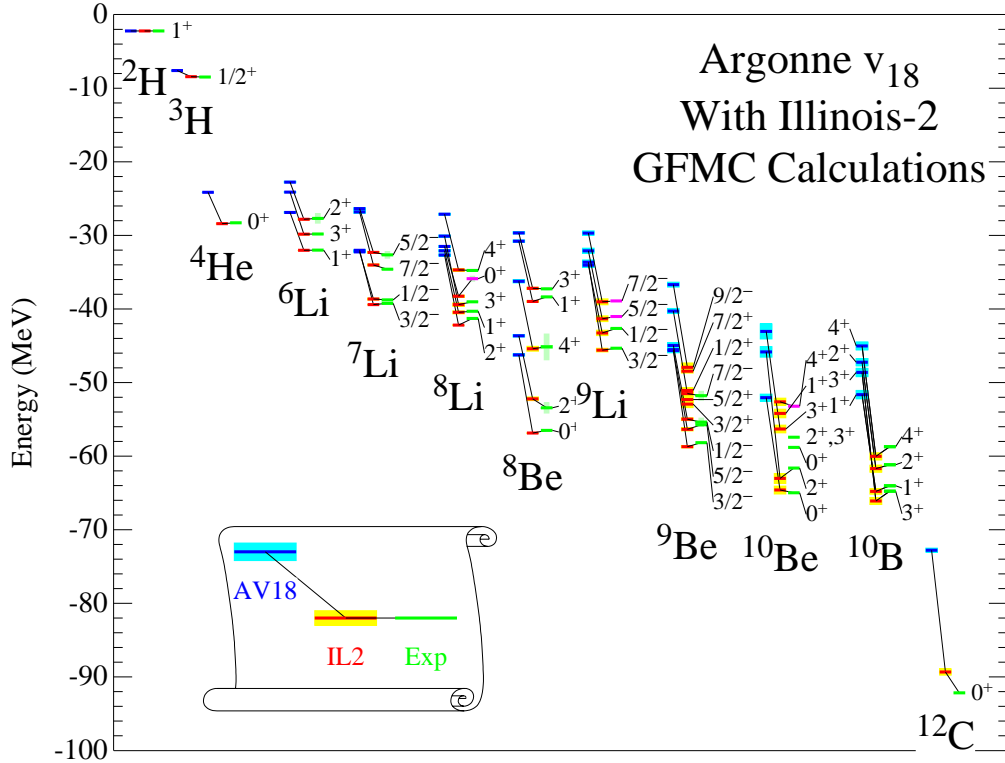


Fig. 3. – GFMC computations of energies for the AV18 and AV18+IL2 Hamiltonians compared with experiment.

2.3. What Makes Nuclear Structure? – We have defined a very complicated nuclear Hamiltonian and it is reasonable to ask if it is all necessary to reproduce the structure of light nuclei. A study [12] was made of this in which features of the nuclear Hamiltonian were systematically removed and the effects on nuclear level energies investigated. For each simplification of the two-nucleon part of H , the remaining terms were readjusted to continue reproducing as many low partial-wave phase shifts, and the deuteron, as possible.

Figure 3 shows the energies of various nuclear states. For each isotope there are three sets of energies: the right-most are the experimental values, the left-most are the results of the GFMC calculations to be described using just the NN potential AV18, and the middle ones are GFMC calculations using the AV18+IL2 Hamiltonian. The AV18+IL2 results are generally in good agreement with the data; the rms deviation is ~ 0.75 MeV. However without the IL2 NNN potential the comparison to data gets steadily worse as the number of nucleons increases. This is a general result that has also been obtained by others using different many-body methods and different NN potentials.

Figure 4 shows the effects of making further simplifications to H beyond removing

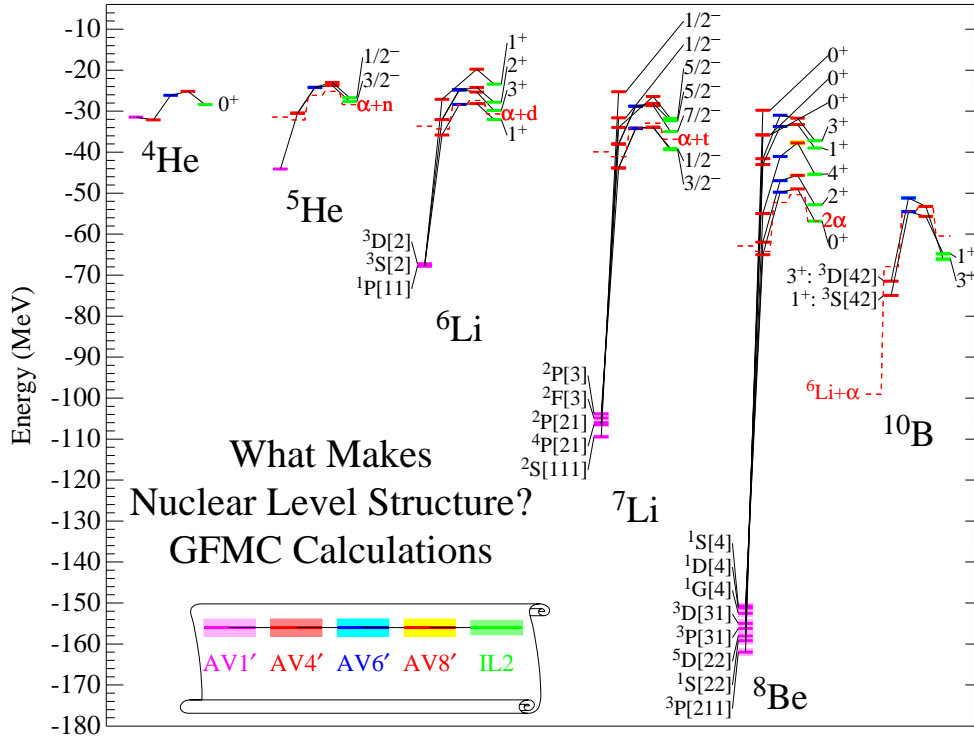


Fig. 4. – Nuclear energy levels for various simplifications of the Hamiltonian

the NNN potential. Here the right-most results are again for the full AV18+IL2 Hamiltonian and thus are close to the data. The next set of results to left are for the AV8' NN potential [13] with no NNN force. With eight operators ($[1, \sigma_i \cdot \sigma_j, S_{ij}, \mathbf{L} \cdot \mathbf{S}] \otimes [1, \tau_i \cdot \tau_j]$), AV8' can reproduce AV18 results for eight partial waves; these are chosen to be 1S_0 , 3S_1 , 3D_1 , ϵ_1 , 1P_1 , and $^3P_{0,1,2}$, (ϵ_1 is the 3S_1 - 3D_1 mixing angle). (Strictly speaking, the 3P_2 potential of AV18 is reproduced but, because the 3F_2 and ϵ_2 potentials are different from those of AV18, the 3P_2 phase shifts are not reproduced.) This potential is more attractive in nuclei than AV18 and more than makes up for the lost binding due to the removal of the NNN potential. In general it gives a good qualitative picture of nuclear energies.

To the left of the AV8' results are results for AV6' which does not have $L \cdot S$ terms. Not surprisingly, these have only negligible spin-orbit splittings. In addition $^6,7\text{Li}$ are essentially unbound to breakup into $\alpha+d$ or $\alpha+t$ (the dashed lines show the indicated thresholds for each Hamiltonian). The next simplification is AV4' which contains no tensor force. With this force, the deuteron no longer has a D state but still has the correct binding energy. The 1S_0 , 3S_1 , 1P_1 , and an average 3P_J partial waves of AV18 are reproduced. This simplified force results in spurious degeneracies of nuclear levels and

somewhat overbinds all the shown nuclei. In particular ${}^8\text{Be}$ is bound against breakup into two alpha particles – an important failure because bound ${}^8\text{Be}$ would result in very different stellar nucleosynthesis.

Finally the left-most results are for AV1', a pure central force that is an average of the 1S_0 and 3S_1 potentials of AV18. This produces an “upside-down” spectrum in which states with the least spatial symmetry are most bound. More importantly, there is no nuclear saturation; each increase in A results in much more binding and there are no $A=5,8$ mass gaps which are essential to big-bang nucleosynthesis and stellar evolution.

Ref. [12] shows results for several other Hamiltonians including an AV2' that contains only central and space-exchange terms and thus is very similar to the popular Volkov potentials [14]. Besides erroneously binding the dineutron, this potential has the strange feature of binding ${}^6\text{He}$ but not ${}^6\text{Li}$ so that $A=6$ beta decay would be in the wrong direction. The conclusion of this study is that one needs almost the full, complicated, Hamiltonian to do realistic nuclear physics.

3. – Quantum Monte Carlo Methods

The many-body problem with the full Hamiltonian described above is very difficult as is indicated by the slow progress over the last half-century that is outlined in the introduction. We need to solve

$$(17) \quad \begin{aligned} \mathcal{H} \Psi(\vec{r}_1, \vec{r}_2, \dots, \vec{r}_A; s_1, s_2, \dots, s_A; t_1, t_2, \dots, t_A) \\ = E \Psi(\vec{r}_1, \vec{r}_2, \dots, \vec{r}_A; s_1, s_2, \dots, s_A; t_1, t_2, \dots, t_A), \end{aligned}$$

where $s_i = \pm\frac{1}{2}$ are nucleon spins, and $t_i = \pm\frac{1}{2}$ are nucleon isospins (proton or neutron). Thus we need to solve the equivalent of $2^A \times \binom{A}{Z}$ complex coupled second-order equations in $3A - 3$ variables (the number of isospin states can be reduced; see Sec.4'2). For ${}^{12}\text{C}$ this corresponds to 270,336 coupled equations in 33 variables.

Furthermore, the coupling is strong; the expectation value of the tensor component of v^π [Eq. 3] is approximately 60% of the total $\langle v_{ij} \rangle$ but it is identically zero if there are no tensor correlations. Thus we cannot perturbatively introduce the couplings.

We use two successive quantum Monte Carlo (QMC) methods to solve this problem. The first is variational Monte Carlo (VMC) in which a trial wave function, containing variational parameters, is posited and the expectation value of the Hamiltonian computed using Monte Carlo integration. In practice we have not been able to formulate accurate enough trial wave functions and so the second step, Green's function Monte Carlo (GFMC), is needed to iteratively project the exact eigenfunction out of the trial wave function. These two methods are described in the following sections. School and review articles on these methods are Refs. [15, 16, 17]. Detailed descriptions may be found in Refs. [18, 13, 19, 20, 21].

4. – Variational Monte Carlo

In VMC we start with a trial wave function, Ψ_T , which contains a number of variational parameters. We vary these parameters to minimize the expectation value of H ,

$$(18) \quad E_T = \frac{\langle \Psi_T | H | \Psi_T \rangle}{\langle \Psi_T | \Psi_T \rangle} \geq E_0 .$$

As indicated, the resulting E_T is, by the Raleigh-Ritz variational principle, greater than the true ground-state energy for the quantum numbers (J^π , J_z , T , and T_z) of Ψ_T . A simplified form of our trial wave functions is

$$(19) \quad |\Psi_T\rangle = [\mathcal{S} \prod_{i<j} (1 + U_{ij} + \sum_k U_{ijk})] \prod_{i<j} f_c(r_{ij}) |\Phi\rangle .$$

Here $f_c(r)$ is a central (mostly short-ranged repulsion) correlation, U_{ij} are non-commuting two-body correlations induced by v_{ij} , and U_{ijk} is a simplified three-body correlation from V_{ijk} .

More specifically,

$$(20) \quad U_{ij} = \sum_{p=2,6} u_p(r_{ij}) O_{ij}^p ,$$

contains $\tau_i \cdot \tau_j$, $\sigma_i \cdot \sigma_j$, $\sigma_i \cdot \sigma_j \tau_i \cdot \tau_j$, S_{ij} , and $S_{ij} \tau_i \cdot \tau_j$ operators, of which the $S_{ij} \tau_i \cdot \tau_j$ is most important due to the already noted strong tensor contribution from v^π . The $f_c(r)$ and $u_p(r)$ are solutions of coupled differential equations with v_{ij} as input [18].

The Φ (see below) is fully antisymmetric; hence the rest of Eq. (19) must be symmetric. But the U_{ij} do not commute; for example

$$(21) \quad [\sigma_1 \cdot \sigma_2, \sigma_1 \cdot \sigma_3] = 2i \sigma_1 \cdot (\sigma_2 \times \sigma_3) .$$

The symmetrizer \mathcal{S} fixes this by summing over all $[\frac{A(A-1)}{2}]!$ permutations of the ordering in $\prod_{i<j}$. In practice this is done by using just one Monte Carlo chosen ordering per wave function evaluation.

4.1. The one-body part of Ψ_T , Φ . – The one-body part of Ψ_T , Φ , is a $1\hbar\omega$ shell-model wave function. It determines the quantum numbers of the state being computed and is fully antisymmetric. For ${}^3\text{H}$ and ${}^{3,4}\text{He}$, Φ can be antisymmetrized in just spin-isospin space, for example

$$(22) \quad |\Phi({}^3\text{H}, M_J = \frac{1}{2})\rangle = \frac{1}{\sqrt{6}} (|p\uparrow n\uparrow n\downarrow\rangle - |p\uparrow n\downarrow n\uparrow\rangle + |n\downarrow p\uparrow n\uparrow\rangle \\ - |n\uparrow p\uparrow n\downarrow\rangle + |n\uparrow n\downarrow p\uparrow\rangle - |n\downarrow n\uparrow p\uparrow\rangle) .$$

For $A > 4$ we need P -wave radial wave functions in order to antisymmetrize Φ ; the antisymmetrization is achieved by summing over all partitions of the A nucleons into four S -shell nucleons (the α core) and $A-4$ P -shell nucleons which are antisymmetrically coupled to J^π and T . To make Φ translationally invariant, we express all functions of single-particle positions as functions of position relative to the center of mass of the A nucleons or of some sub-cluster of them. The one-body wave functions are solutions of Woods Saxon potentials containing several variational parameters. If desired the separation energy of these one-body wave functions can be fixed at the experimental value to guarantee that the Ψ_T has the correct asymptotic form. In general Φ has several spatial-symmetry components depending on how many ways a state of the desired quantum numbers can be constructed in the P -shell basis. For example the ${}^6\text{Li}$ Φ have the form

$$(23) \quad |\Phi\rangle = \mathcal{A} \sum_{LS} \beta_{LS} |\Phi_6(LSJMTT_3)_{1234:56}\rangle ,$$

$$(24) \quad \Phi_6(LSJMTT_3)_{1234:56} = \Phi_4(0000)_{1234} \phi_p^{LS}(R_{\alpha 5}) \phi_p^{LS}(R_{\alpha 6}) \\ \left\{ [Y_{1m_l}(\Omega_{\alpha 5}) Y_{1m'_l}(\Omega_{\alpha 6})]_{LM_L} \times [\chi_5(\frac{1}{2}m_s) \chi_6(\frac{1}{2}m'_s)]_{SM_S} \right\}_{JM} \\ \times [\nu_5(\frac{1}{2}t_3) \nu_6(\frac{1}{2}t'_3)]_{TT_3} .$$

A $1\hbar\omega$ LS -basis diagonalization determines the β_{LS} .

4.2. Representing Ψ_T in the computer. – The wave function, $\Psi_T(\vec{r}_1, \vec{r}_2, \dots, \vec{r}_A)$, is a complex vector in spin-isospin space with dimension $[N_S \text{ components for spin}] \times [N_T \text{ components for isospin}]$. The number of spin states is 2^A . However for even A , if we choose to use $M_J = 0$, we can calculate and retain only half the spin vector, say that part with positive spin for the last nucleon, and obtain the other half of the vector by time-reversal symmetry. The number of isospin states, N_T , depends on the isospin basis being used:

$$(25) \quad N_T = \binom{A}{Z} \quad \text{for a proton-neutron basis ,}$$

$$(26) \quad = \frac{2T+1}{A/2+T+1} \binom{A}{A/2+T} \quad \text{for a good isospin basis .}$$

Potentials (v_{ij} , V_{ijk}) and correlations (u_{ij} , U_{ijk}) involve repeated operations on Ψ . For example $\sigma_i \cdot \sigma_j$ may be written as

$$(27) \quad \sigma_i \cdot \sigma_j = 2(\sigma_i^+ \sigma_j^- + \sigma_i^- \sigma_j^+) + \sigma_i^z \sigma_j^z$$

$$(28) \quad = 2P_{ij}^\sigma - 1$$

$$(29) \quad = \begin{pmatrix} 1 & 0 & 0 & 0 \\ 0 & -1 & 2 & 0 \\ 0 & 2 & -1 & 0 \\ 0 & 0 & 0 & 1 \end{pmatrix} \text{ acting on } \begin{pmatrix} \uparrow\uparrow \\ \uparrow\downarrow \\ \downarrow\uparrow \\ \downarrow\downarrow \end{pmatrix}.$$

Here P_{ij}^σ exchanges the spin of i and j . Consider the spin part of an $A=3$ wave function; $\sigma_i \cdot \sigma_j$ will not mix different isospin components and, for different i and j , will separately act on different, non-contiguous, 4-element blocks of Ψ :

$$(30) \quad \Psi = \begin{pmatrix} a_{\uparrow\uparrow\uparrow} \\ a_{\uparrow\uparrow\downarrow} \\ a_{\uparrow\downarrow\uparrow} \\ a_{\uparrow\downarrow\downarrow} \\ a_{\downarrow\uparrow\uparrow} \\ a_{\downarrow\uparrow\downarrow} \\ a_{\downarrow\downarrow\uparrow} \\ a_{\downarrow\downarrow\downarrow} \end{pmatrix}; \quad \sigma_1 \cdot \sigma_2 \Psi = \begin{pmatrix} a_{\uparrow\uparrow\uparrow} \\ a_{\uparrow\uparrow\downarrow} \\ 2a_{\downarrow\uparrow\uparrow} - a_{\uparrow\downarrow\uparrow} \\ 2a_{\downarrow\uparrow\downarrow} - a_{\uparrow\downarrow\downarrow} \\ 2a_{\uparrow\downarrow\uparrow} - a_{\downarrow\uparrow\uparrow} \\ 2a_{\uparrow\downarrow\downarrow} - a_{\downarrow\uparrow\downarrow} \\ a_{\downarrow\downarrow\uparrow} \\ a_{\downarrow\downarrow\downarrow} \end{pmatrix};$$

$$(31) \quad \sigma_2 \cdot \sigma_3 \Psi = \begin{pmatrix} a_{\uparrow\uparrow\uparrow} \\ 2a_{\uparrow\downarrow\uparrow} - a_{\uparrow\uparrow\downarrow} \\ 2a_{\uparrow\uparrow\downarrow} - a_{\uparrow\downarrow\uparrow} \\ a_{\uparrow\downarrow\downarrow} \\ a_{\downarrow\uparrow\uparrow} \\ 2a_{\downarrow\downarrow\uparrow} - a_{\uparrow\downarrow\downarrow} \\ 2a_{\downarrow\uparrow\downarrow} - a_{\downarrow\downarrow\uparrow} \\ a_{\downarrow\downarrow\downarrow} \end{pmatrix}; \quad \sigma_3 \cdot \sigma_1 \Psi = \begin{pmatrix} a_{\uparrow\uparrow\uparrow} \\ 2a_{\downarrow\uparrow\uparrow} - a_{\uparrow\uparrow\downarrow} \\ a_{\uparrow\uparrow\downarrow} \\ 2a_{\downarrow\downarrow\uparrow} - a_{\uparrow\downarrow\downarrow} \\ 2a_{\uparrow\uparrow\downarrow} - a_{\downarrow\uparrow\uparrow} \\ a_{\downarrow\uparrow\downarrow} \\ 2a_{\uparrow\downarrow\downarrow} - a_{\downarrow\uparrow\uparrow} \\ a_{\downarrow\downarrow\downarrow} \end{pmatrix}.$$

Similarly, the tensor operator is

$$(32) \quad S_{ij} = 3 \sigma_i \cdot \hat{r}_{ij} \sigma_j \cdot \hat{r}_{ij} - \sigma_i \cdot \sigma_j$$

$$(33) \quad = 3 \begin{pmatrix} z^2 - 1/3 & z(x - iy) & z(x - iy) & (x - iy)^2 \\ z(x + iy) & -z^2 - 1/3 & x^2 + y^2 - 2/3 & -z(x - iy) \\ z(xiy) & x^2 + y^2 - 2/3 & -z^2 + 1/3 & -z(x - iy) \\ (x + iy)^2 & -z(x + iy) & -z(x + iy) & z^2 - 1/3 \end{pmatrix},$$

where $x = x_i - x_j$, etc. As shown in Eqs. (30) and (31), these 4×4 matrices form a sparse matrix of (non-contiguous) 4×4 blocks in the A -body problem. Specially coded subroutines are used to efficiently perform these operations.

Most of the time in VMC or GFMC calculations is spent evaluating wave functions (or in GFMC making a propagation step which is equivalent). The pair operators dominate this time. The evaluation of a kinetic energy involves numerical second derivatives which require $6A$ wave function computations. Hence the product of A , the number of pairs, and of the length of the spin-isospin vector is a good indication of how the total computational

	A	Pairs	Spin \times Isospin	$\prod(/{}^8\text{Be})$
${}^4\text{He}$	4	6	8×2	0.001
${}^5\text{He}$	5	10	32×5	0.020
${}^6\text{Li}$	6	15	32×5	0.036
${}^7\text{Li}$	7	21	128×14	0.66
${}^8\text{Be}$	8	28	128×14	1.
${}^8\text{Li}$	8	28	128×28	2.
${}^9\text{Be}$	9	36	512×42	18.
${}^{10}\text{B}$	10	45	512×42	24.
${}^{10}\text{Be}$	10	45	512×90	51.
${}^{11}\text{B}$	11	55	2048×132	400.
${}^{12}\text{C}$	12	66	2048×132	530.
${}^{16}\text{O}$	16	120	32768×1430	224,000.
${}^{40}\text{Ca}$	40	780	$3.6\times 10^{21} \times 6.6\times 10^9$	2.8×10^{20}
${}^8\text{n}$	8	28	128×1	0.071
${}^{14}\text{n}$	14	91	8192×1	26.

TABLE I. – *Scaling of wave function computation time*

time scales with A . Table I shows this scaling for various nuclei, assuming $M=0$ for even J nuclei and that good-isospin bases are being used. The final column shows the product of the first three columns relative to ${}^8\text{Be}$. We can do calculations up to $A=10$ routinely and a few ${}^{12}\text{C}$ calculations have been done. It is clear that this approach is not reasonable for ${}^{16}\text{O}$. The last two lines are for “neutron drops” for which isospin does not have to be considered. This allows somewhat bigger A to be reached.

4.3. A Variational Monte Carlo Calculation. – The basic steps in a variational calculation are

- Generate a random position: $\mathbf{R} = \vec{r}_1, \vec{r}_2, \dots, \vec{r}_A$.
- Make many (1000’s) random steps based on the probability $P = |\Psi_T(\mathbf{R})|^2$.
- Start integration loop:
 - Make order 10 steps based on P .
 - Compute and sum $H_{\text{local}}(\mathbf{R}) = [\Psi_T(\mathbf{R})^\dagger H \Psi_T(\mathbf{R})] / |\Psi_T(\mathbf{R})|^2$. Gradients and Laplacians are computed by differences: $6A$ evaluations of $\Psi_T(\mathbf{R} + \delta_j \vec{r}_i)$.
- $\langle \Psi_T | H | \Psi_T \rangle / \langle \Psi_T | \Psi_T \rangle = \text{average}(H_{\text{local}})$.

A random step from a given position, \mathbf{R} , to a new position \mathbf{R}' is made using the Metropolis method:

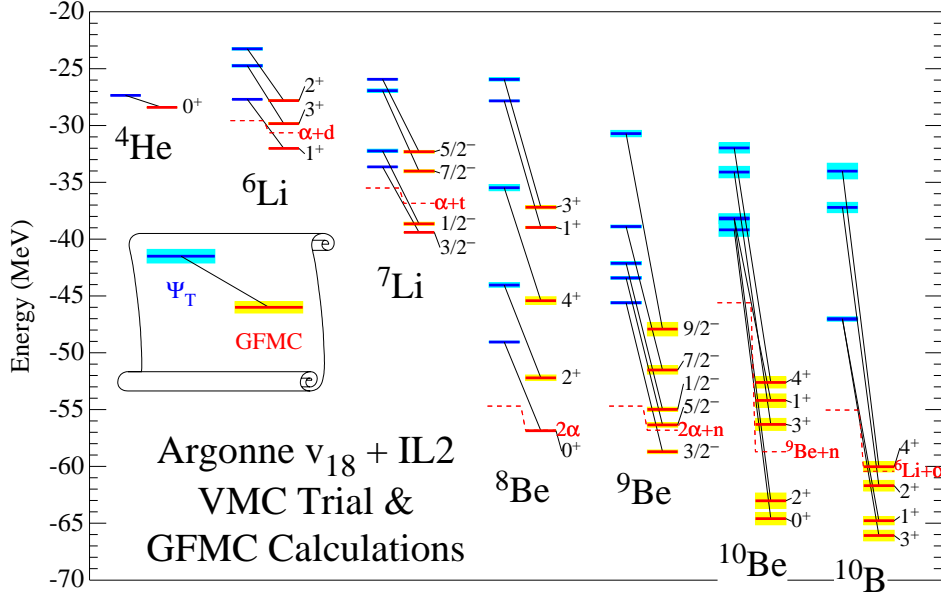


Fig. 5. – Comparison of VMC and GFMC energies for the AV18+IL2 Hamiltonian. The light shading shows Monte Carlo statistical errors.

- Use $3A$ uniform random numbers on $(0,1)$, $\{w_j\}$, to make $\Delta\mathbf{R}$; $\Delta x_i = 2\delta r(w_j - 1)$.
- Set $\mathbf{R}' = \mathbf{R} + \Delta\mathbf{R}$, and compute $P(\Delta\mathbf{R}) = |\Psi_T(\mathbf{R}')|^2 / |\Psi_T(\mathbf{R})|^2$.
- Make another random number on $(0,1)$: p
- If $P > p$, the step is accepted; replace \mathbf{R} with \mathbf{R}' .
if $P < p$, the step is rejected; discard \mathbf{R}' and stay at \mathbf{R} .

4.4. Accuracy of VMC energies. – Figure 5 compares VMC energies of various nuclear states with the corresponding GFMC values for the AV18+IL2 Hamiltonian. As is described in the next section, the GFMC results are believed to be accurate to 1–2%. For ${}^4\text{He}$ the VMC result is quite close to the GFMC. However as we move into the P shell, the VMC results get steadily worse. In fact, although the GFMC calculations show that this Hamiltonian binds the nuclei shown with the exception of ${}^8\text{Be}$, the VMC energies are all above the VMC energies for the subclusters that the nuclei can breakup into. Furthermore the ${}^8\text{Be}$ VMC energy is actually lower than those of 9- and 10-body nuclei. Calculations with simpler Hamiltonians show that these failures of the VMC energies are related to the tensor force; VMC calculations for the simple AV4' potential discussed in Sec. 2.3 are quite accurate, while those for AV6' have significant errors.

5. – Green’s Function Monte Carlo – General Description

As shown above, our VMC trial wave functions are not good enough for P -shell nuclei. This means that they contain admixtures of excited-state components in addition to the desired exact ground-state component, Ψ_0 ;

$$(34) \quad \Psi_T = \Psi_0 + \sum \alpha_i \Psi_i .$$

We use Green’s Function Monte Carlo to project Ψ_0 out of Ψ_T by propagating in imaginary time, τ :

$$(35) \quad \Psi(\tau) = \exp[-(H - \tilde{E}_0)\tau] \Psi_T ,$$

$$(36) \quad = e^{-(E_0 - \tilde{E}_0)\tau} \times [\Psi_0 + \sum \alpha_i e^{-(E_i - E_0)\tau} \Psi_i] ,$$

$$(37) \quad \lim_{\tau \rightarrow \infty} \Psi(\tau) \propto \Psi_0 ,$$

where \tilde{E}_0 is a guess for the exact E_0 .

The eigenvalue E_0 is calculated exactly while other expectation values are generally calculated neglecting terms of order $|\Psi_0 - \Psi_T|^2$ and higher. In contrast, the error in the variational energy, E_T , is of order $|\Psi_0 - \Psi_T|^2$, and other expectation values calculated with Ψ_T have errors of order $|\Psi_0 - \Psi_T|$.

The evaluation of $\Psi(\tau)$ is made by introducing a small time step, $\Delta\tau$, $\tau = n\Delta\tau$,

$$(38) \quad \Psi(\tau) = \left[e^{-(H - E_0)\Delta\tau} \right]^n \Psi_T = G^n \Psi_T .$$

where G is the short-time Green’s function. The $\Psi(\tau)$ is represented by a vector function of \mathbf{R} , and the Green’s function, $G_{\alpha\beta}(\mathbf{R}', \mathbf{R})$ is a matrix function of \mathbf{R}' and \mathbf{R} in spin-isospin space, defined as

$$(39) \quad G_{\alpha\beta}(\mathbf{R}', \mathbf{R}) = \langle \mathbf{R}', \alpha | e^{-(H - E_0)\Delta\tau} | \mathbf{R}, \beta \rangle .$$

It is calculated with leading errors of order $(\Delta\tau)^3$ as discussed below. Omitting spin-isospin indices for brevity, $\Psi(\mathbf{R}_n, \tau)$ is given by

$$(40) \quad \Psi(\mathbf{R}_n, \tau) = \int G(\mathbf{R}_n, \mathbf{R}_{n-1}) \cdots G(\mathbf{R}_1, \mathbf{R}_0) \Psi_T(\mathbf{R}_0) d\mathbf{P} ,$$

and

$$(41) \quad E(\tau) = \frac{\int \Psi_T^\dagger(\mathbf{R}_n) G^\dagger(\mathbf{R}_n, \mathbf{R}_{n-1}) \cdots G^\dagger(\mathbf{R}_1, \mathbf{R}_0) H \Psi_T(\mathbf{R}_0) d\mathbf{P}}{\int \Psi_T^\dagger(\mathbf{R}_n) G^\dagger(\mathbf{R}_n, \mathbf{R}_{n-1}) \cdots G^\dagger(\mathbf{R}_1, \mathbf{R}_0) \Psi_T(\mathbf{R}_0) d\mathbf{P}} ,$$

where $d\mathbf{P} = d\mathbf{R}_0 d\mathbf{R}_1 \cdots d\mathbf{R}_n$. Here we have placed the $\Psi(\tau)$ to the left side of H because the derivatives in H may be evaluated only on Ψ_T ; we cannot compute gradients or Laplacians of $\Psi(\tau)$. This $3An$ -dimensional integral is computed by Monte Carlo.

5.1. The Short-Time Propagator. – The success of a GFMC calculation depends on an accurate and fast evaluation of the short-time propagator, $G_{\alpha\beta}(\mathbf{R}', \mathbf{R})$. One wants to be able to do this for the largest possible value of $\Delta\tau$ to reduce the number of steps, n , needed to reach some asymptotic value of τ . The most important features of $\Psi(\tau)$ are induced by the NN potential, so consider first $G_{\alpha\beta}(\mathbf{R}', \mathbf{R})$ for a Hamiltonian with no NNN potential. This can be written as

$$(42) \quad G_{\alpha\beta}(\mathbf{R}', \mathbf{R}) = e^{\tilde{E}_0 \Delta\tau} G_0(\mathbf{R}', \mathbf{R}) \langle \alpha | \left[\mathcal{S} \prod_{i < j} \frac{g_{ij}(\mathbf{r}'_{ij}, \mathbf{r}_{ij})}{g_{0,ij}(\mathbf{r}'_{ij}, \mathbf{r}_{ij})} \right] | \beta \rangle ,$$

where

$$(43) \quad G_0(\mathbf{R}', \mathbf{R}) = \langle \mathbf{R}' | e^{-K \Delta\tau} | \mathbf{R} \rangle = \left[\sqrt{\frac{m}{2\pi\hbar^2 \Delta\tau}} \right]^{3A} \exp \left[\frac{-(\mathbf{R}' - \mathbf{R})^2}{2\hbar^2 \Delta\tau / m} \right] ,$$

is the many-nucleon free propagator and $g_{0,ij}$ is the corresponding two-nucleon free propagator,

$$(44) \quad g_{0,ij}(\mathbf{r}'_{ij}, \mathbf{r}_{ij}) = \left[\sqrt{\frac{\mu}{2\pi\hbar^2 \Delta\tau}} \right]^3 \exp \left[-\frac{(\mathbf{r}'_{ij} - \mathbf{r}_{ij})^2}{2\hbar^2 \Delta\tau / \mu} \right] ,$$

and $\mu = m/2$ is the reduced mass.

The $G_0(\mathbf{R}', \mathbf{R})$ is included in the Monte Carlo integration [Eq. (41)] by using it to make the step from \mathbf{R} to \mathbf{R}' . The magnitudes of the $3A$ steps (x , y , and z for each nucleon) are determined by sampling a Gaussian of the width given in Eq. (43) and the directions of the steps are picked by importance sampling; see Ref. [13] for details.

Eq. (42) introduces the exact two-body propagator,

$$(45) \quad g_{ij}(\mathbf{r}'_{ij}, \mathbf{r}_{ij}) = \langle \mathbf{r}'_{ij} | e^{-H_{ij} \Delta\tau} | \mathbf{r}_{ij} \rangle ,$$

$$(46) \quad H_{ij} = -\frac{\hbar^2}{m} \nabla_{ij}^2 + v_{ij} .$$

All terms containing any number of the same v_{ij} and K are treated exactly in this propagator, as we have included the imaginary-time equivalent of the full two-body scattering amplitude. Eq. (42) still has errors of order $(\Delta\tau)^3$, however they are from commutators of terms like $v_{ij} K v_{ik} (\Delta\tau)^3$ which become large only when both pairs ij and ik are close.

To calculate g_{ij} , we use the techniques developed by Schmidt and Lee[22] for scalar interactions. These allow g_{ij} to be calculated with high (~ 10 digit) accuracy. However, this calculation is quite time consuming. Therefore, prior to the GFMC calculation, we compute and store the the propagator on a grid. For a spin-independent interaction, the propagator g_{ij} would depend only upon the two magnitudes r' and r and the angle $\cos(\theta) = \hat{\mathbf{r}}' \cdot \hat{\mathbf{r}}$ between them. Here, though, there is also a dependence upon the spin

quantization axis. Rotational symmetry allows one to calculate the spin-isospin components of $g_{ij}(\mathbf{r}', \mathbf{r})$ for any \mathbf{r}' and \mathbf{r} by simple SU3 spin rotations and values of g_{ij} on a grid of initial points $\mathbf{r} = (0, 0, z)$ and final points $\mathbf{r}' = (x', 0, z')$. In addition, the fact that the propagator is Hermitian allows us to store only the values for $z > z'$.

Returning to the full Hamiltonian including NNN forces, the complete propagator is given by

$$(47) \quad G_{\alpha\beta}(\mathbf{R}', \mathbf{R}) = e^{E_0\Delta\tau} G_0(\mathbf{R}', \mathbf{R}) \exp\left[-\sum (V_{ijk}^R(\mathbf{R}') + V_{ijk}^R(\mathbf{R})) \frac{\Delta\tau}{2}\right] \\ \langle\alpha|I_3(\mathbf{R}')|\gamma\rangle\langle\gamma|\left[\mathcal{S}\prod_{i<j}\frac{g_{ij}(\mathbf{r}'_{ij}, \mathbf{r}_{ij})}{g_{0,ij}(\mathbf{r}'_{ij}, \mathbf{r}_{ij})}\right]|\delta\rangle\langle\delta|I_3(\mathbf{R})|\beta\rangle,$$

with

$$(48) \quad I_3(\mathbf{R}) = \left[1 - \frac{\Delta\tau}{2} \sum V_{ijk}^{2\pi}(\mathbf{R})\right].$$

The exponential of $V_{ijk}^{2\pi}$ is expanded to first order in $\Delta\tau$ thus, there are additional error terms of the form $V_{ijk}^{2\pi}V_{i'j'k'}^{2\pi}(\Delta\tau)^2$. However, they have negligible effect since $V_{ijk}^{2\pi}$ has a magnitude of only a few MeV. It was verified that the results for ${}^4\text{He}$ do not show any change, outside of statistical errors, when $\Delta\tau$ is decreased from 0.5 GeV^{-1} .

5.2. Problems with Nuclear GFMC. – While GFMC is in principal exact for the $\langle H \rangle$, there are several practical difficulties that make it only approximate. We have made many tests of the accuracy of the GFMC energies, both by comparison to other methods and by comparing calculations with different $\Delta\tau$, starting Ψ_T , and other computational parameters. These tests show that our results for energy are good to $\sim 1\%$ up to $\sim 2\%$ for larger A or $N - Z$ (${}^8\text{He}$ is particularly difficult). Some of the problems are:

5.2.1. Limitation on H . The exact propagator of Eq. (46) can be computed for the full v_{18} potential, however the \mathbf{L}^2 and $(\mathbf{L} \cdot \mathbf{S})^2$ terms in the potential correspond to state-dependent changes of the mass appearing in the free Green's function. Since we do not know how to sample such a free Green's function, we cannot use the exact g_{ij} for the full potential, but rather must use one constructed for an approximately equivalent potential that does not contain quadratic \mathbf{L} terms, namely the AV8' introduced in Sec. 2.3. The difference between the desired and approximate potentials is computed perturbatively. Comparisons with more accurate calculations for ${}^3\text{H}$ and ${}^4\text{He}$ suggest that this introduces errors of less than 1%.

5.2.2. Fermion sign problem. The $G(\mathbf{R}_i, \mathbf{R}_{i-1})$ is a local operator and can mix in the boson solution. This has a (much) lower energy than the fermion solution and thus is exponentially amplified in subsequent propagations. In the final integration with the antisymmetric Ψ_T , the desired fermionic part is projected out in Eq. (41), but in the presence of large statistical errors that grow exponentially with τ . Because the number

of pairs that can be exchanged grows with A , the sign problem also grows exponentially with increasing A . For $A \geq 8$, the errors grow so fast that convergence in τ cannot be achieved.

For simple scalar wave functions, the fermion sign problem can be controlled by not allowing the propagation to move across a node of the wave function. Such “fixed-node” GFMC provides an approximate solution which is the best possible variational wave function with the same nodal structure as Ψ_T . However, a more complicated solution is necessary for the spin- and isospin-dependent wave functions of nuclei. This is provided by “constrained-path” propagation in which those configurations that, in future generations, will contribute only noise to expectation values are discarded. If the exact ground state $|\Psi_0\rangle$ were known, any configuration at time step n for which

$$(49) \quad \Psi(\mathbf{R}_n)^\dagger \Psi_0(\mathbf{R}_n) = 0 ,$$

where a sum over spin-isospin states is implied, could be discarded. The sum of these discarded configurations can be written as a state $|\Psi_d\rangle$, which obviously has zero overlap with the ground state. The Ψ_d contains only excited states and should decay away as $\tau \rightarrow \infty$, thus discarding it is justified. Of course the exact Ψ_0 is not known, and so configurations are discarded with a probability such that the average overlap with the trial wave function,

$$(50) \quad \langle \Psi_d | \Psi_T \rangle = 0 .$$

Many tests of this procedure have been made [19] and it usually gives results that are consistent with unconstrained propagation, within statistical errors. However a few cases in which the constrained propagation converges to the wrong energy (either above or below the correct energy) have been found. Therefore a small number, $n_u = 10$ to 20, of unconstrained steps are made before evaluating expectation values. These few unconstrained steps, out of typically 400 total steps, appear to be enough to damp out errors introduced by the constraint, but do not greatly increase the statistical error. Unfortunately, the constrained-path $E(\tau)$ are not upper bounds to the true E_0 ; examples have been found in which the constrained energies evaluated with inadequate n_u are below E_0 .

5.2.3. Mixed estimates extrapolation. As shown in Eq. (41), GFMC computes “mixed” expectation values between Ψ_T and $\Psi(\tau)$ of operators,

$$(51) \quad \langle O \rangle_{\text{Mixed}} = \frac{\langle \Psi(\tau) | O | \Psi_T \rangle}{\langle \Psi(\tau) | \Psi_T \rangle} .$$

The desired expectation values, of course, have $\Psi(\tau)$ on both sides. By writing $\Psi(\tau) = \Psi_T + \delta\Psi(\tau)$ and neglecting terms of order $[\delta\Psi(\tau)]^2$, we obtain the approximate expression

$$(52) \quad \langle O(\tau) \rangle = \frac{\langle \Psi(\tau) | O | \Psi(\tau) \rangle}{\langle \Psi(\tau) | \Psi(\tau) \rangle} \approx \langle O(\tau) \rangle_{\text{Mixed}} + [\langle O(\tau) \rangle_{\text{Mixed}} - \langle O \rangle_T] ,$$

	$\langle O \rangle_T$	$\langle O \rangle_{\text{Mix}}$	$\langle O \rangle_{\text{Mix}} - \langle O \rangle_T$	$\langle O \rangle$
K	146.60	153.49	6.89	160.39
v_{nuc}	-171.64	-180.49	-8.85	-189.34
v_C	1.53	1.54	0.01	1.55
V_{ijk}	-4.10	-6.43	-2.34	-8.77
Sum	-27.61	-31.90	-4.28	-36.17
H	-27.61	-31.90	—	-31.90

TABLE II. – Contributions to $\langle H \rangle$ for ${}^6\text{Li}$ (MeV)

where $\langle O \rangle_T$ is the variational expectation value. More accurate evaluations of $\langle O(\tau) \rangle$ are possible, essentially by measuring the observable at the mid-point of the path. However, such estimates require a propagation twice as long as the mixed estimate and require separate propagations for every $\langle O \rangle$ to be evaluated.

The expectation value of the Hamiltonian is a special case. The $\langle H(\tau) \rangle_{\text{Mixed}}$ can be re-expressed as [23]

$$(53) \quad \langle H(\tau) \rangle_{\text{Mixed}} = \frac{\langle \Psi_T | e^{-(H-E_0)\tau/2} H e^{-(H-E_0)\tau/2} | \Psi_T \rangle}{\langle \Psi_T | e^{-(H-E_0)\tau/2} e^{-(H-E_0)\tau/2} | \Psi_T \rangle} \geq E_0 ,$$

since the propagator $\exp[-(H-E_0)\tau]$ commutes with the Hamiltonian. Thus $\langle H(\tau) \rangle_{\text{Mixed}}$ is already the correct expectation value and must not be extrapolated. This results in the unfortunate circumstance that the sum of the pieces of $\langle H \rangle$ is not equal to the full GFMC value of $\langle H \rangle$. An example is shown in Table II which shows VMC, mixed, and extrapolated energies for ${}^6\text{Li}$ computed with the AV18+IL2 Hamiltonian. The sum of the extrapolated kinetic and potential energy values is 4.3 MeV different from the total energy. This means that the extrapolated values of the pieces have errors whose absolute sum is at least this big.

Instead of the linear extrapolation of Eq. (52), one can also use a ratio extrapolation:

$$(54) \quad \langle O(\tau) \rangle \approx \frac{\langle O(\tau) \rangle_{\text{Mixed}}^2}{\langle O \rangle_T} ,$$

which is the same as Eq. (52) to lowest order in $[\langle O(\tau) \rangle_{\text{Mixed}} - \langle O \rangle_T]$, but obviously has different quadratic errors. This method has the feature that if both $\langle O(\tau) \rangle_{\text{Mixed}}$ and $\langle O \rangle_T$ have the same sign, then the extrapolated $\langle O(\tau) \rangle$ will also have that sign. This is an advantage for quantities such as densities (see Sec. 8) which must be positive; if the GFMC is reducing the density at large r where it is exponentially falling, linear extrapolation can result in negative values. Of course such large extrapolations by either method are uncertain.

5.3. A Simplified GFMC Calculation. – The basic steps in a GFMC calculation are

- Start with collection of $\Psi(\tau=0, \mathbf{R}_j) = \Psi_T(\mathbf{R}_j)$ from a VMC calculation
- Loop over time steps $\tau_n = n\Delta\tau$
 - Loop over configurations j
 - * Make a random step to $\mathbf{R}'_j = \mathbf{R}_j + \Delta\mathbf{R}_j$ by sampling $G_0(\mathbf{R}', \mathbf{R})$
 - * Sample several directions based on simplified Ψ_T and potential
 - * Compute $\Psi(\tau_{n+1}, \mathbf{R}'_j) = G(\mathbf{R}'_j, \mathbf{R}_j)\Psi(\tau_n, \mathbf{R}_j)$
 - * Possibly mark as killed due to the constraint $\Psi^\dagger(\tau_{n+1}, \mathbf{R}'_j) \cdot \Psi_T(\mathbf{R}'_j)$
 - * Use importance sampling to kill or replicate the configuration $\Psi(\tau_{n+1}, \mathbf{R}'_j)$
 - Every 20–40 time steps
 - * Compute the local energy $\Psi^\dagger(\tau_n, \mathbf{R}_j)H\Psi_T(\mathbf{R}_j)/\Psi^\dagger(\tau_n, \mathbf{R}_j)\Psi_T(\mathbf{R}_j)$
 - * Check that total number of configurations is staying reasonably constant

GFMC calculations are quite computer intensive. For example, a typical ${}^8\text{Li}$ calculation requires 300 processor hours running at a delivered (not theoretical-peak) speed of one GigaFLOPS. As shown in Table I, a ${}^{10}\text{B}$ calculation will need about 10 times this and ${}^{12}\text{C}$ 250 times it. Clearly such calculations are practical only on highly parallel computers. Our GFMC program uses a master-slave structure in which each slave gets a number of configurations to propagate as outlined in the preceding paragraph. The computed energy results are sent back to master for averaging as they are generated.

Because configurations are multiplied or killed during propagation, the work load fluctuates. It is important to periodically rebalance the work load – otherwise slaves will wind up with nothing to do while the last slave with the biggest work load finishes its calculations. To do this, the master periodically collects load statistics and then tells slaves to redistribute some of their configurations. The slaves have work (energy calculations left from previous time steps) set aside to do during this synchronization. This method results in parallelization efficiencies of typically 95% on up to 2000 processors. However, the next generation of large computers will have 10,000 to 100,000 processors, which is more than the number of configurations to be propagated for a large nucleus like ${}^{12}\text{C}$. Thus the program has to be made parallel at a finer level; this is being worked on.

5.4. Examples of GFMC propagation. – Figure 6 shows the $E(\tau)$ as a function of the imaginary time, τ , for the beginning of GFMC propagation for ${}^4\text{He}$. The propagation starts from the VMC value of -26.92 MeV, and initially decreases rapidly with increasing τ ; essentially converged values are achieved by $\tau = 0.01$ MeV $^{-1}$. The propagation is continued another factor of 10 to $\tau = 0.1$ MeV $^{-1}$ and the results averaged over the last half of the propagation to get the converged result of $-28.300(15)$ MeV. The curve is a fit of the form

$$(55) \quad E(\tau) = E_0 + \frac{\sum_i \alpha_i^2 E_i^* \exp(-E_i^* \tau)}{1 + \sum_i \alpha_i^2 \exp(-E_i^* \tau)},$$

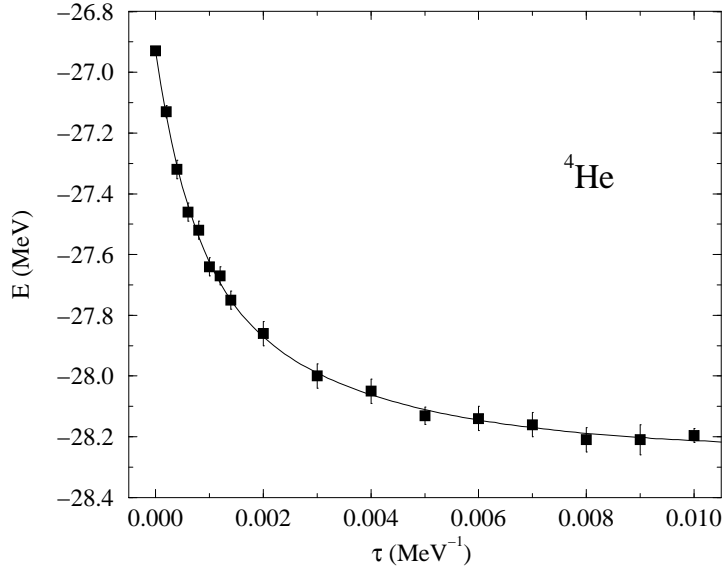


Fig. 6. – GFMC propagation for ${}^4\text{He}$. The $E(\tau)$ is shown as a function of imaginary time, τ .

to the computed $E(\tau)$ using three terms. The E_1^* was fixed at the first 0^+ excitation energy of 20.2 MeV of ${}^4\text{He}$, and the other two E_i^* and the three α_i were varied in the fit. The fitted E_i^* turn out to be very large, 340 and 1480 MeV, with small α_i , 0.0018 and 0.00046, respectively. Thus the errors in the VMC Ψ_T correspond to small amounts of extremely high excitation energy; GFMC is particularly efficient at filtering out such errors.

Figure 7 shows GFMC propagation, using the AV18+IL2 Hamiltonian, of the ground, first 3^+ , and 2^+ states of ${}^6\text{Li}$. The propagation for the ground state (which is particle stable with this H) and the 3^+ (which is only slightly above the $d+\alpha$ threshold and experimentally has a narrow width) is stable after $\tau = 0.2 \text{ MeV}^{-1}$. However the 2^+ (a broad resonance) never becomes stable; the $E(\tau)$ are decaying to the threshold energy of separated α and d clusters. Because the 3^+ state $E(\tau)$ stops decreasing around $\tau=0.2$, the $E(\tau=0.2)$, shown by the star, is best GFMC estimate we can currently make of the resonance energy. However it is now possible to make GFMC calculations using scattering-wave boundary conditions (see Sec. 7) and this method will be applied to states such as ${}^6\text{Li}(2^+)$.

6. – Results for energies of nuclear states

Figure 3 compares the GFMC energies of various nuclear states with experiment and Fig. 8 does the same for excitation energies. In both cases the left set of bars for each isotope shows results using just the AV18 NN potential while the middle set of bars is for

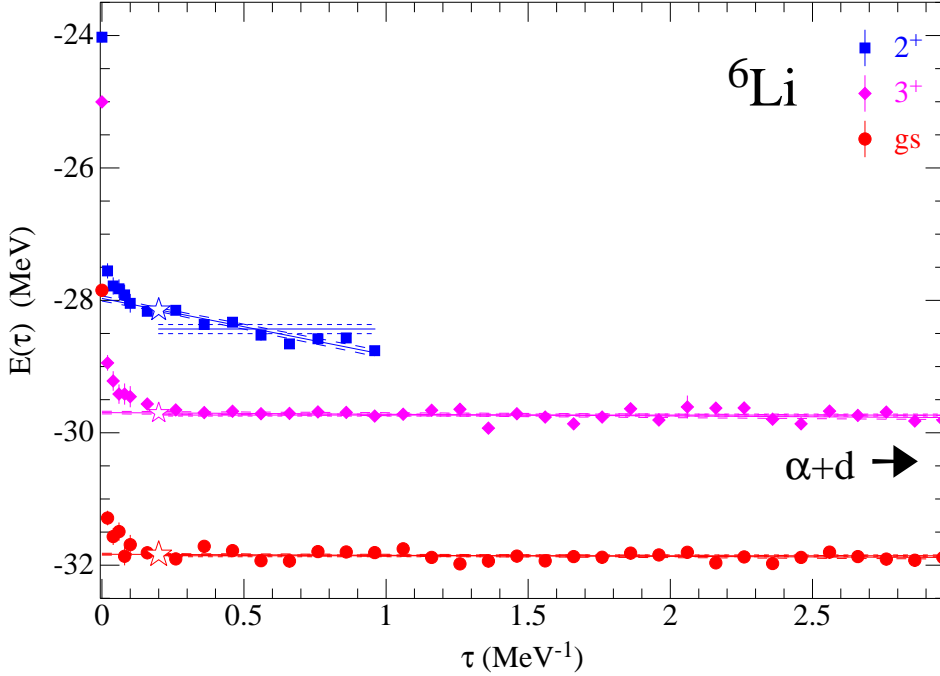


Fig. 7. – GFMC propagation for three states of ${}^6\text{Li}$.

the full AV18+IL2 Hamiltonian. As has already been observed, AV18 alone significantly underbinds all nuclei except the deuteron; including IL2 results in fairly good agreement with the experimental values. The excitation spectra in Fig. 8 show that IL2 also fixes other problems that arise when just a NN potential is used. For example, spin-orbit splittings are usually too small without the NNN potential (note the $\frac{1}{2}^- - \frac{3}{2}^-$ and $\frac{5}{2}^- - \frac{7}{2}^-$ splittings in ${}^7\text{Li}$ and the $\frac{1}{2}^- - \frac{3}{2}^-$ splitting in ${}^9\text{Li}$). As is discussed in the next subsection, even the ordering of states can be changed by the NNN potential.

The discussion of Sec. 5 implies that GFMC can be used only for the lowest state of each set of quantum numbers but Fig. 3 shows several states with the same J^π . The ability of GFMC to provide such results was demonstrated in Ref. [21].

6.1. Ordering of States in ${}^{10}\text{Be}$ and ${}^{10}\text{B}$. – Figure 9 shows the beginning of the computed and experimental excitation spectra of ${}^{10}\text{Be}$ and ${}^{10}\text{B}$. We see that NN potentials with no NNN predict a 1^+ ground state for ${}^{10}\text{B}$ while the Illinois-2 NNN potential fixes this and gives the correct 3^+ ground state. No-core shell model calculations show that other NN potentials without NNN potentials also give a 1^+ ground state for ${}^{10}\text{B}$ [24], so this is not a failure of just AV18. This incorrect ground-state prediction is another manifestation of too-small spin-orbit splitting using just NN potentials; in 1956 D. Kurath showed that the relative positions of the 3^+ and 1^+ levels depends on the amount of spin-orbit strength in a shell-model calculation [25].

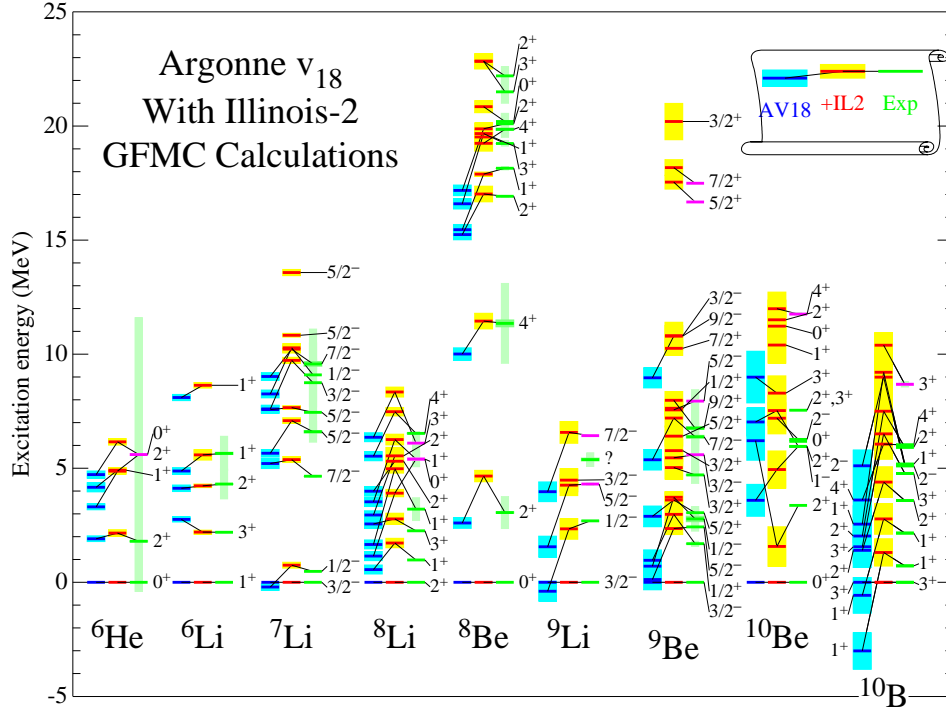


Fig. 8. – Gfmc computations of excitation energies for the AV18 and AV18+IL2 Hamiltonians compared with experiment. The shading on the experimental energies shows the widths of resonances.

The first two excited states in ^{10}Be are both 2^+ and Fig. 9 shows that including the IL2 NNN potential reverses their order. VMC and Gfmc calculations predict large positive and negative quadrupole moments (Q) for these states; with no NNN potential, the Gfmc energy of the $Q > 0$ state is the lower, while adding the IL2 NNN potential reverses this. VMC also predicts a large $B(E2)$ to the g.s. for only the state with $Q > 0$. An ATLAS experiment for the $B(E2)$ and quadrupole moments of these states will be made to determine if the reversal of order given by IL2 is correct.

6.2. Charge Dependence and Isospin Mixing. – The differences of the energies of states in the same isomultiplet are a probe of isospin-breaking components of the Hamiltonian. The largest such component is the Coulomb potential between protons, but it has been known since 1969 that this does not fully account for the measured differences [26]; the discrepancy is referred to as the Nolen-Schiffer anomaly. It is convenient to parametrize the energies of the isomultiplets by the coefficients $a_{A,T}^{(n)}$,

$$(56) \quad E_{A,T}(T_z) = \sum_{n \leq 2T} a_{A,T}^{(n)} Q_n(T, T_z) ,$$

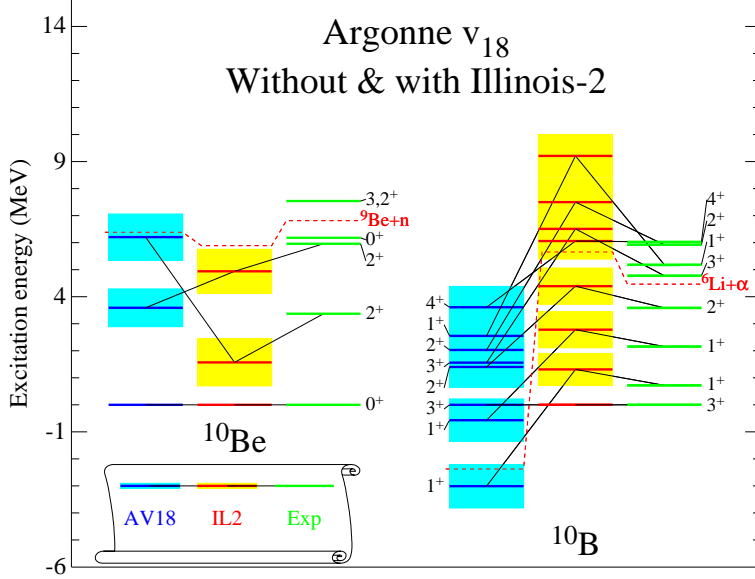


Fig. 9. – Excitation energies of ^{10}Be and ^{10}B

where $Q_0 = 1$ is the isoscalar component, $Q_1 = T_z$ the isovector, and $Q_2 = \frac{1}{2}(3T_z^2 - T^2)$ the isotensor. Term 18 of AV18 contributes to the isovector component and terms 15 to 17 to the isotensor component; both terms receive contributions from the various electromagnetic terms in AV18. Table III shows computed and experimental values of the coefficients for several isomultiplets; the $v^{\text{CSB+CD}}$ column gives contribution of the nuclear (strong-interaction) terms in AV18, while the K^{CSB} column shows that resulting from the difference of the proton and neutron masses. In general the non-Coulomb electromagnetic and strong charge symmetry breaking and charge dependent terms result in good agreement with the experimental values and thus resolve the Nolen-Schiffer anomaly.

Figure 10 shows the beginning of the experimental excitation spectrum of ^8Be . From 16 to 19 MeV excitation there are pairs of 2^+ , 1^+ , and 3^+ levels with isospin 0 and 1. The two 2^+ levels are very close and hence strongly isospin mixed; the 3^+ levels also have significant mixing. The mixing has been experimentally known from the decay properties of the states since 1966 [27]. However, as with the Nolen Schiffer anomaly, calculations using just Coulomb mixing underestimate the amount of mixing. Table IV shows GFMC calculations using AV18+IL2 of the mixing matrix elements for the three pairs [28]. The contribution of the nuclear CSB term is relatively more important here than for the Nolen Schiffer anomaly. The agreement of the predictions with the data is not as satisfactory as for the Nolen Schiffer anomaly. The final line of the table shows the mixing matrix element between the first 2^+ (at 3 MeV) state and the isospin-1 17-MeV state. The small value of this matrix element, and the large energy denominator, shows

	T	n	v^{Coul}	v^{otherEM}	$v^{\text{CSB+CD}}$	K^{CSB}	Total	Expt.
${}^3\text{H}-{}^3\text{He}$	$\frac{1}{2}$	1	649	29	64	14	757	764
${}^7\text{Li}-{}^7\text{Be}$	$\frac{1}{2}$	1	1458	40	83	23	1605	1644
${}^7\text{He}, {}^7\text{Li}^*, {}^7\text{Be}^*, {}^7\text{B}$	$\frac{3}{2}$	1	1286	14	49	17	1366	1373
	$\frac{3}{2}$	2	132	7	34		174	175
${}^8\text{Li}, {}^8\text{Be}^*, {}^8\text{B}$	1	1	1692	24	78	24	1818	1770
	1	2	140	5	-5		140	145
${}^8\text{He}, {}^8\text{Li}^*, {}^8\text{Be}^*, {}^8\text{B}^*, {}^8\text{C}$	2	1	1719	13	83	26	1840	1659
	2	2	153	7	42		203	153

TABLE III. – Computed (*AV18+IL2*) and experimental Nolen-Schiffer energies for several isomultiplets

that the first 2^+ state has very little $T = 1$ contamination; this is important to the possibility of using ${}^8\text{Li}(\beta^-){}^8\text{Be}(1^{\text{st}} 2^+)$ decay as a test of $V - A$.

6.3. Can Modern Nuclear Hamiltonians Tolerate a Bound Tetraneutron? – In 2002 a claimed observation of a bound tetraneutron was published [29, 30]. The experiment did

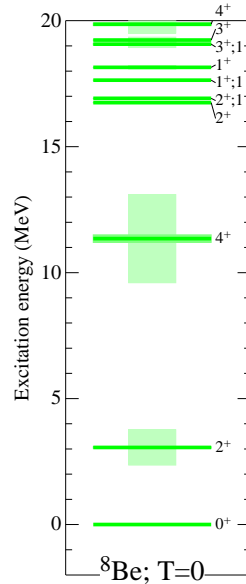


Fig. 10. – Experimental spectrum of ${}^8\text{Be}$

J^P	GFMC				Expt
	Coulomb	Strong CSB	Other	Total	
$2^{nd} 2^+$	78	21	16	115	144
1^+	80	18	4	102	120
3^+	61	15	14	90	63
$1^{st} 2^+$	4	0.4	1	6	-

TABLE IV. – Isospin mixing matrix elements for ${}^8\text{Be}$ in keV

not produce a definite binding energy, just the statement that four neutrons are weakly bound. It is well known that the dineutron is not bound, but rather has low-energy pole on the second sheet (pseudo bound state); AV18 along with other realistic potentials has this feature. A set of GFMC calculations were made to see if the AV18+IL2 Hamiltonian, or acceptable modifications of it, could reproduce the tetra-neutron claim [31]. It was clearly established that the unmodified AV18+IL2 does not bind ${}^4\text{n}$; at most there is some weak resonance at $E \sim +2$. MeV.

Minimal modifications to AV18+IL2 to give $E({}^4\text{n}) \sim -0.5$ MeV were then made

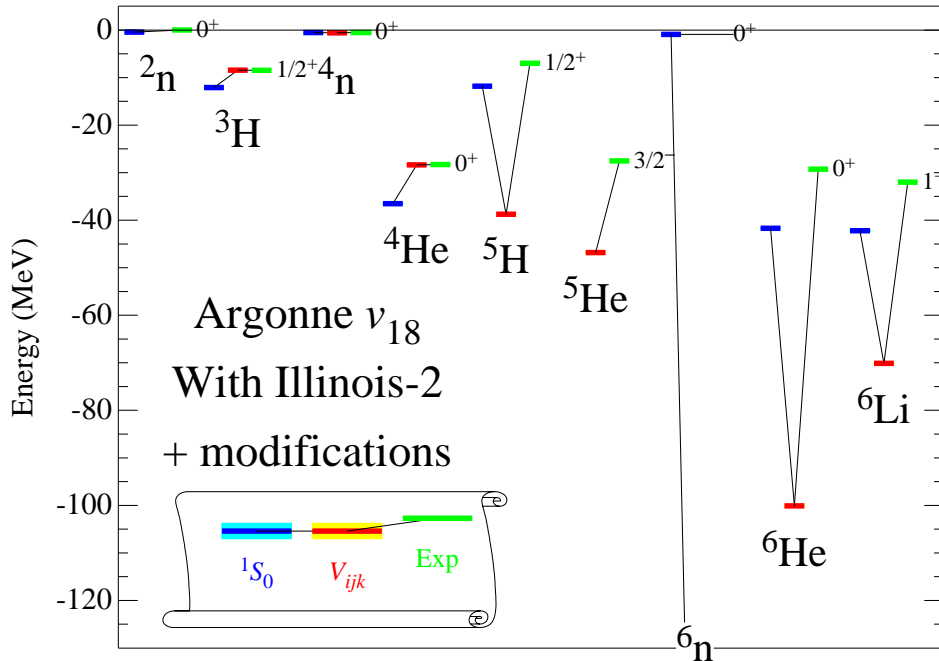


Fig. 11. – Nuclear energies with Hamiltonians modified to bind a tetra-neutron

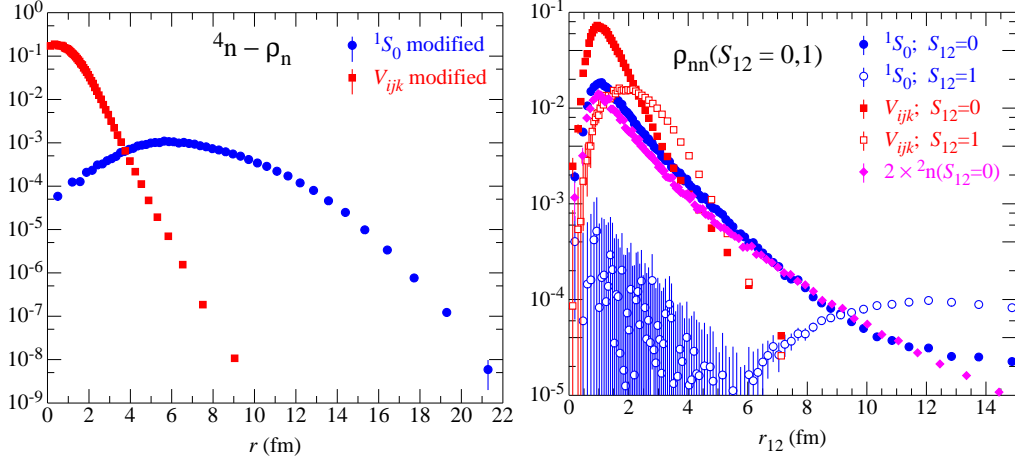


Fig. 12. – One-body (left) and two-body (right) densities of tetra-neutrons. Circles are for the 1S_0 NN and squares for the $T = \frac{3}{2}$ NNN modifications; the diamonds are for 2n .

and the effects of such modifications on the energies of other, well established, nuclei were computed. Figure 11 shows some of these. In the first case (the left-hand bars), the intermediate-range part of the 1S_0 partial-wave potential in of AV18 was increased enough to bind four neutrons. This increase results in the dineutron also being bound, in fact the 4n is still unbound against breakup into two dineutrons in this model. As the figure shows, other existing nuclei (^3H , ^4He , etc.) all become significantly over bound with this increased 1S_0 potential. Also 6n and 8n (not shown) become bound. An attempt to bind the 4n by changing the 3P_J part of AV18 was also made, but this requires a huge change which very strongly overbinds other nuclei.

A second attempt was to add an attractive $V_{ijk}(T = \frac{3}{2})$ to H . This has two advantages: 1) it has no effect on NN scattering and does not make a bound 2n ; 2) because the modification is made only in isospin- $\frac{3}{2}$ triples, it has no effect on ^3H , ^3He , or ^4He ; these have only isospin- $\frac{1}{2}$ triples. However, as can be seen in the figure, as soon as this potential can act (i.e. in nuclei with $T = \frac{3}{2}$ triples), it produces huge overbinding. The most dramatic effect is in pure neutron systems: 6n is bound by 220 MeV and 8n by 650 MeV. These are the most stable 6- and 8-nucleon systems with this Hamiltonian, so all other 6- and 8-body nuclei would beta decay to them!

Finally an attractive four-nucleon, $T = 2$, potential was added (not shown). This does not effect ^6Li but does very strongly overbind ^6He , larger nuclei, and pure neutron systems with more than four neutrons. The conclusion of the study is that a bound 4n is incompatible with our understanding of nuclear forces. In the meantime the experiment has not been successfully reproduced.

The 1S_0 NN and $T = \frac{3}{2}$ NNN modifications have very different effects on $A > 4$ binding energies, even though both have been adjusted to bind 4n by only 0.5 MeV; the NNN modification results in much more severe overbinding. Figure 12 helps to

explain this. The left panel shows the one-body densities of the two bound ${}^4\text{n}$ systems; the 1S_0 NN modification results in a very diffuse ${}^4\text{n}$ with a rms radius of 8.9 fm. The right panel shows the pair density which is proportional to finding two neutrons a given distance apart. For the 1S_0 NN modification, the density for a $S=0$ pair is peaked around 1 fm and is very similar to the pair distribution of the isolated ${}^2\text{n}$ which is bound by this potential. The $S=1$ pair distribution is peaked at 12 fm; it arises from neutrons in different dineutron clusters. Thus this ${}^4\text{n}$ looks like two widely separated dineutrons. The binding comes from the small tails where neutrons from each dineutron get close enough to interact. The change of $v_{NN}({}^1S_0)$ needed to achieve this is not that big and hence bigger nuclei overbound only somewhat.

On the other hand, a V_{NNN} requires all three neutrons in a triple to be close together to be effective. Thus the $T = \frac{3}{2}$ NNN modification must bring the two dineutrons close together. This results in the much more compact one-body density, with a rms radius of only 1.9 fm, shown in the left panel and a two-body density that is much sharper than the isolated ${}^2\text{n}$. The $V_{NNN}(T = \frac{3}{2})$ must be large to achieve this high density and it thus has a large effect in all bigger nuclei.

7. – GFMC for Scattering States

The GFMC calculations presented so far have treated the nucleus as a particle-stable system; that is the starting wave function, Ψ_T , is exponentially decaying as any nucleon is removed to a large distance from the center of mass. However many of the states of interest are particle unstable; they are above the threshold for emission of a single nucleon or, as is often the case for light nuclei, the threshold for breakup into subclusters. This approximation appears to be adequate for narrow resonances which have only a small scattering-wave component. However broad resonances should really be computed with proper scattering-wave boundary conditions; as shown in Fig. 7 we do not achieve a converged energy for a broad state with the bound-state GFMC. In addition to being the correct approach, scattering solutions allow one to compute the phase shift as a function of energy and thus obtain the width of the resonance. Finally, one might also be interested in the phase shifts for partial waves that have no resonance.

Preliminary GFMC calculations of neutron-alpha scattering were made in 1991 [32], but detailed, high statistics results have been obtained only recently [33]. Instead of using exponentially decaying wave functions, we construct Ψ_T to have a specified logarithmic derivative, γ , at some large boundary radius ($R \geq 7$ fm). Here R is the maximum distance that any nucleon is allowed to get from the other $A - 1$ nucleons. The GFMC propagation uses a method of images to preserve γ at R , and thus finds $E(R, \gamma)$; the eigenenergy that corresponds to the boundary condition. The phase shift, $\delta(E)$, can then be computed from R , γ , and $E(R, \gamma)$. This procedure is repeated for a number of γ and $\delta(E)$ is mapped out parametrically.

Figure 13 shows an example of this for the broad $\frac{1}{2}^-$ resonance in ${}^5\text{He}$. The bound-state boundary condition does not give a stable energy, but is decaying to the $n+{}^4\text{He}$ threshold energy. The scattering boundary condition produces a stable energy; the value

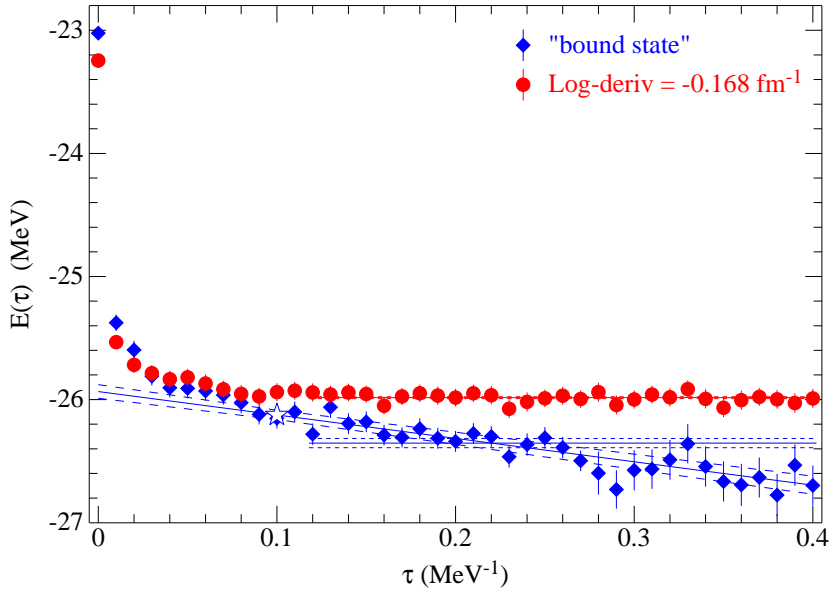


Fig. 13. – GFMC propagation for ${}^5\text{He}(\frac{1}{2}^-)$ using bound- and scattering-state boundary conditions (diamonds and circles, respectively).

of γ used in this example results in an energy slightly above the resonance energy.

Figure 14 compares the calculations of $n+\alpha$ scattering with a R -matrix analysis of the data [34] (solid curves). The left panel shows the partial-wave phase shifts computed for three different Hamiltonians: AV18 with no V_{ijk} , AV18+IL2, and AV18+UIX (UIX is an older NNN potential [35] that, with AV18, correctly binds ${}^3\text{H}$ and ${}^4\text{He}$, but underbinds P -shell nuclei). All three Hamiltonians give very similar results for the $\frac{1}{2}^+$ partial wave which has no resonance. However only the AV18+IL2 correctly reproduces the two P -wave partial waves; AV18 alone misses both of them and AV18+UIX fits the $\frac{1}{2}^-$ partial wave but has too-small spin-orbit splitting and misses the $\frac{3}{2}^-$ one. The right panel shows the partial-wave cross sections for the AV18+IL2 Hamiltonian. The strong resonance in the $\frac{3}{2}^-$ channel is very well reproduced showing that both the position and width of the resonance agree with the data; the much broader $\frac{1}{2}^-$ resonance is also well reproduced. In addition the good agreement with the low-energy $\frac{1}{2}^+$ cross section data shows that the scattering length is reproduced.

This first study is very promising; the GFMC method, with its ability to have correct asymptotic forms, should be applied to other scattering calculations including a number of broad resonances [${}^7,{}^9\text{He}$, ${}^6\text{Li}(2^+)$, ${}^8\text{Be}(2^+,4^+)$, *etc.*] and the initial states of astrophysically interesting capture reactions [${}^4\text{He}(d,\gamma){}^6\text{Li}$, ${}^7\text{Be}(p,\gamma){}^8\text{B}$, *etc.*].

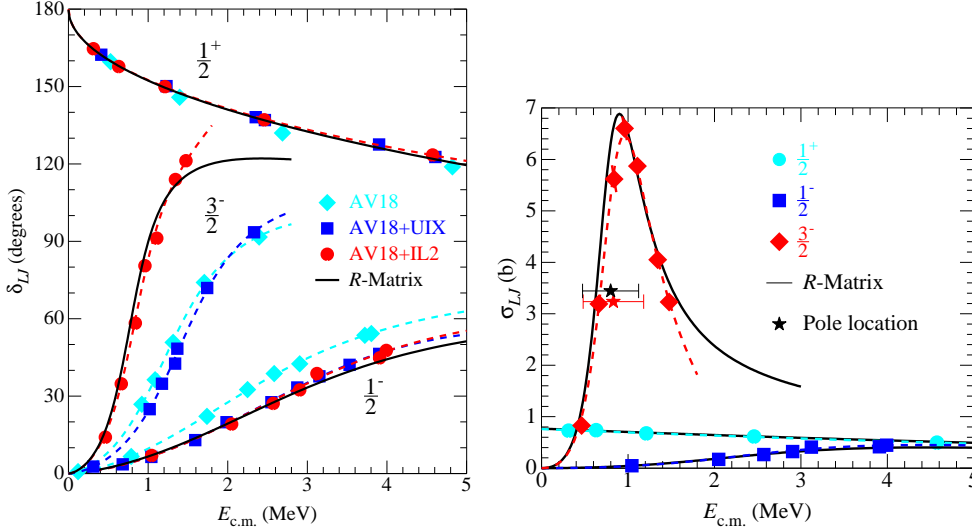


Fig. 14. – GFMC calculations of $n + \alpha$ scattering in the three principal partial waves. The left panel shows partial-wave phase shifts for three Hamiltonians. The right panel shows corresponding partial-wave cross sections for the AV18+IL2 Hamiltonian. The experimental data is represented by the solid curves.

8. – Coordinate- and momentum-space densities

Up to now we have been concentrating on GFMC calculations of energies of nuclear states. However matrix elements of any operator may be evaluated in the GFMC propagation by using the extrapolation formulas, Eqs. (52) or (54). I discuss some recent work on the charge radii, the corresponding densities, and momentum-space densities in this section.

8.1. RMS radii and one-body densities of helium isotopes. – A few years ago, a group at Argonne measured the RMS charge radius of the radioactive nucleus ${}^6\text{He}$ (β -decay half-life 0.8 sec.) with the remarkable accuracy of 0.7% [36] and the corresponding measurement for ${}^8\text{He}$ (β -decay half-life 0.1 sec.) will be published soon [37]. This has led us to attempt equally precise GFMC calculations of the corresponding point proton RMS radii. Such calculations are very difficult because of the small separation energies of the two valence neutrons in these isotopes ($E_{\text{sep}} = 0.97$ MeV for ${}^6\text{He}$ and 2.14 MeV for ${}^8\text{He}$). Changes in the starting Ψ_T and other aspects of the GFMC calculations can result in changes of 200 keV (400 keV for ${}^8\text{He}$) in the computed energy (and hence E_{sep}). The RMS radius depends strongly on E_{sep} ; as E_{sep} goes to zero, the radius goes to infinity. Thus we cannot give a precise value for the computed RMS radius for a specific Hamiltonian. Instead we find that the computed values for the same Hamiltonian with different GFMC calculations, or even for different Hamiltonians, all lie in a band

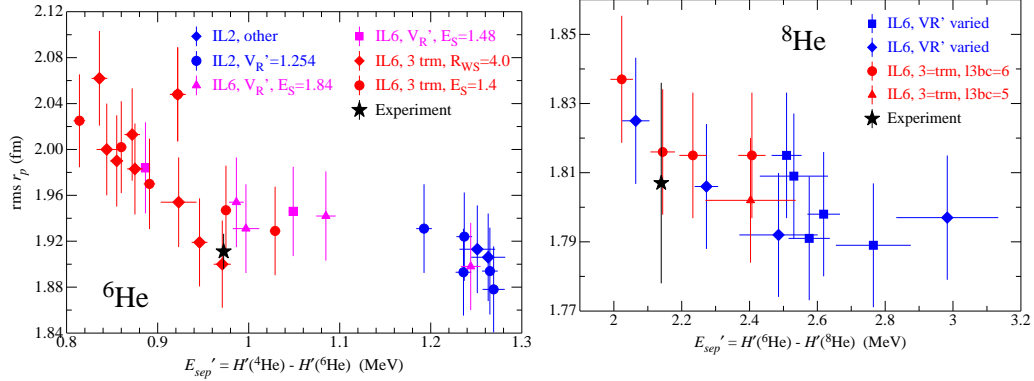


Fig. 15. – GFMC calculations of point proton RMS radii of ${}^6,8\text{He}$ plotted as a function of the two-neutron separation energy obtained in the calculation.

of radius versus separation energy. This is shown in Fig. 15 which shows results for two Hamiltonians, AV18+IL2 and AV18+IL6, each with several GFMC calculations (IL6 is a newer, unpublished, version of IL2). The stars in each panel show the experimental point radii at the experimental separation energies; they are clearly consistent with our calculations which give 1.92(4) fm for ${}^6\text{He}$ and 1.82(2) fm, for ${}^8\text{He}$. These numbers are both significantly bigger than the RMS point radius of ${}^4\text{He}$ which is 1.46 fm.

Figure 16 shows the point proton and neutron densities of ${}^4,6,8\text{He}$. The alpha particle is extremely compact; its central density is twice that of nuclear matter. In these calculations it has identical proton and neutron densities which is a very good approximation. As is shown below, the valence neutrons in ${}^6,8\text{He}$ do not seriously distort the ${}^4\text{He}$ core,

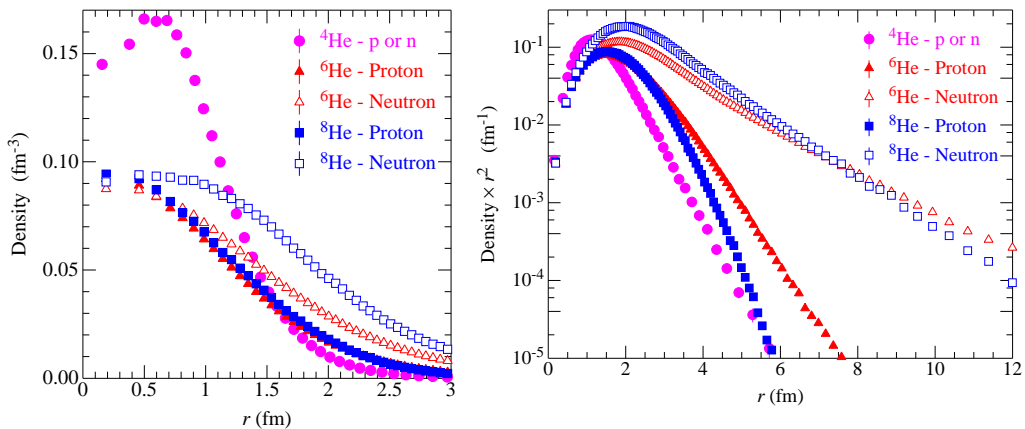


Fig. 16. – GFMC calculations, using AV18+IL2, of proton and neutron point densities for helium isotopes. The left panel shows density on a linear scale; the right panel $r^2\rho$ on a logarithmic scale.

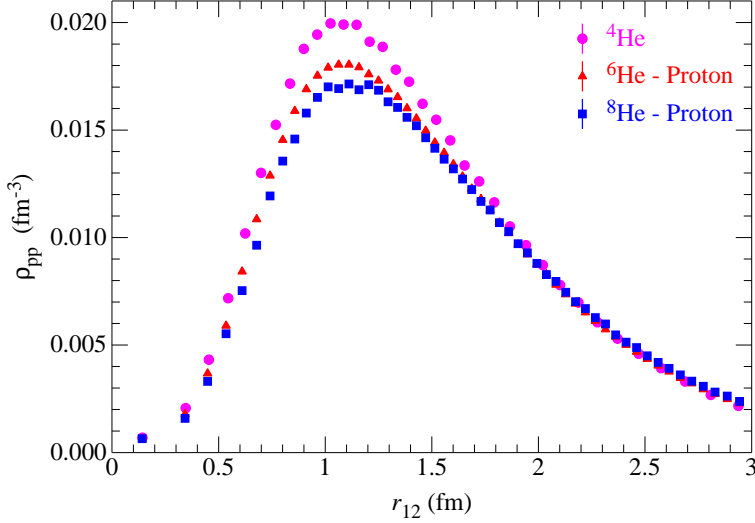


Fig. 17. – GFMC calculations, using AV18+IL2, of two-proton densities of helium isotopes.

rather they just drag the ${}^4\text{He}$ center of mass around. This results in the proton density being spread out which is why the charge radii of ${}^{6,8}\text{He}$ are so much greater than that of ${}^4\text{He}$ even though all three nuclei have just two protons. The right panel of the figures clearly shows that ${}^{6,8}\text{He}$ have large neutron halos due to the weak binding of the extra neutrons. The neutron halo of ${}^6\text{He}$ is more diffuse than that of ${}^8\text{He}$ as is expected from the smaller E_{sep} of ${}^6\text{He}$.

8.2. Is an alpha particle in a sea of neutrons still an alpha particle? – The previous subsection showed that the proton density in ${}^{6,8}\text{He}$ is much more spread out than the density of ${}^4\text{He}$, even though ${}^{6,8}\text{He}$ have only extra neutrons added to a ${}^4\text{He}$ core. This might first be thought to indicate that the core of ${}^{6,8}\text{He}$ has been considerably enlarged by the neutrons. This can be studied by computing ρ_{pp} , the pair density which is proportional to the probability for finding two protons a given density apart. These distribution functions are shown in Fig. 17, again calculated with GFMC for the AV18+IL2 model. These nuclei each have just one pp pair which presumably is in the “alpha core” of ${}^{6,8}\text{He}$. Unlike the one-body densities, these distributions are not sensitive to center of mass effects, and thus if the alpha core of ${}^{6,8}\text{He}$ is not distorted by the surrounding neutrons, all three ρ_{pp} distributions in the figure should be the same.

We see that the pp distribution spreads out slightly with neutron number in the helium isotopes, with an increase of the pair rms radius of approximately 4% in going from ${}^4\text{He}$ to ${}^6\text{He}$, and 8% to ${}^8\text{He}$. While this could be interpreted as a swelling of the alpha core, it might also be due to the charge-exchange ($\tau_i \cdot \tau_j$) correlations which can transfer charge from the core to the valence nucleons. Since these correlations are rather long-ranged, they can have a significant effect on the pp distribution. VMC calculations of ${}^4\text{He}$ with

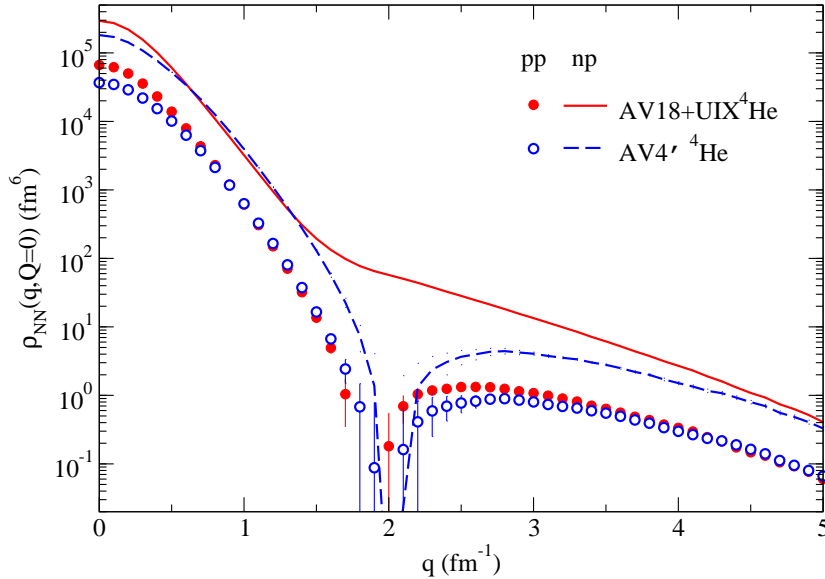


Fig. 18. – Two-nucleon momentum distributions in ${}^4\text{He}$, computed by VMC for the AV18+UIX Hamiltonian. The symbols show pp distributions; the curves are for np .

wave functions modified to give ρ_{pp} distributions close to those of ${}^{6,8}\text{He}$ suggest that the alpha cores of ${}^{6,8}\text{He}$ are excited by ~ 80 and ~ 350 keV, respectively, which corresponds to only a 0.4–2% admixture of the first 0^+ excited state of ${}^4\text{He}$ at 20 MeV. Thus almost all of the increased RMS radius of the proton density is due to the α core of ${}^{6,8}\text{He}$ being pushed around by the neutrons and not distortions of the core.

8.3. Two-nucleon knockout – ($e, e'pN$). – A recent JLAB experiment for ${}^{12}\text{C}(e, e'pN)$ measured back to back pp and np pairs; that is pairs with total C.M. momentum $Q = 0$, as a function of their relative momentum, q [38]. They found that the cross section for np pairs with q in the range $2\text{--}3\text{ fm}^{-1}$ is 10–20 times larger than that for pp pairs in the same range. To study this we made VMC calculations of the corresponding pair momentum distributions (ρ_{NN}) in several nuclei from ${}^3\text{H}$ to ${}^8\text{Be}$ [39]. The calculations for ${}^4\text{He}$ are shown in Fig. 18. Results for the AV18+UIX Hamiltonian (which for $A=3,4$ is a good approximation to AV18+IL2) are shown as the solid line (np pairs) and solid circles (pp pairs). Around $q=2\text{ fm}^{-1}$ there is a deep minimum in the pp density which results in large values for ρ_{np}/ρ_{pp} . The dashed curve and open circles show the corresponding quantities computed for the AV4' NN potential (Sec. 2.3) with no NNN potential; in this case both densities have a deep dip and there is no enhancement of the ratio.

The AV4' potential has no tensor force and thus np pairs are just S -wave while, for the full Hamiltonian, isospin-0 np pairs, like the deuteron, have a D -wave admixture. The S -wave deuteron momentum distribution has a zero at 2 fm^{-1} which is filled in by the D -wave contribution, the same as is seen here for np pairs in ${}^4\text{He}$. The tensor force

is much smaller in the pure $T=1$ pp pairs, so the deep S -wave minimum is not filled in for those pairs, even with the AV18+UIX Hamiltonian. Calculations for ${}^3\text{He}$, ${}^6\text{Li}$, and ${}^8\text{Be}$ all show this effect although the deep minimum is somewhat filled in for ${}^8\text{Be}$. Thus the JLAB experiment shows the importance of tensor correlations up to $> 3 \text{ fm}^{-1}$.

9. – Conclusions

Quantum Monte Carlo methods are powerful tools for studying light nuclei with realistic nuclear interactions. Calculations of $A = 6 - 12$ nuclear energies with accuracies of $1 - 2\%$ are possible and the AV18+IL2 reproduces binding energies with an average error of order 0.7 MeV for $A = 3 - 12$. The NNN potential is required for overall P -shell energies and for spin-orbit splittings and several level orderings.

The QMC methods allow matrix elements of many operators of interest to be computed. This contribution presents rms radii, one- and two-body densities and two-body momentum distributions. These are generally in good agreement with experiment. Recently GFMC values of $A=6,7$ electromagnetic and weak transitions have also been computed; these improve on older VMC calculations and also generally agree with experiment [40]. Another topic not covered here is overlap functions and the related spectroscopic factors; these are used as input to calculations (such as distorted-wave Born approximation) of nuclear reactions; recent results are presented in Refs. [41, 42]. A just-finished interesting study used VMC calculations to investigate the effects on nuclear binding energies of changes in the Hamiltonian induced by changes of the fundamental constants [43].

GFMC calculations are very computer intensive and at present ${}^{12}\text{C}$ can just barely be done. However a new generation of extremely parallel computers is becoming available and we are working with computer scientists to enable the GFMC program to make use of these machines. This should lead to the possibility of detailed studies of ${}^{12}\text{C}$ including second 0^+ (Hoyle) state which is the doorway for triple-alpha burning. This state has resisted precise calculation by shell-model based methods; we hope that our more flexible variational wave functions, combined with GFMC propagation, will overcome these difficulties.

But perhaps the most important advance in nuclear GFMC is the computation of scattering states. In these calculations the correct scattering-wave boundary condition is achieved. The resulting wave functions will be used to compute reactions of astrophysical interest such as ${}^3\text{He}+\alpha \rightarrow {}^7\text{Be}$, $p+{}^7\text{Be} \rightarrow {}^8\text{B}$, and $n+(\alpha+\alpha) \rightarrow {}^9\text{Be}$. Indeed all big-bang nucleosynthesis, solar neutrino, and some r -process seeding reactions are accessible.

* * *

As can be seen from the author lists of the citations, the work reported in this contribution is the result of long-term collaborations with Joesph Carlson (who invented nuclear GFMC), Kenneth M. Nollett (who is doing the GFMC scattering), Vijay R. Pandharipande (who for many years guided and inspired our group), Rocco Schiavilla (who has provided the expertise on the electroweak currents) and Robert B. Wiringa

(who has developed the VMC wave functions). I thank R. B. Wiringa for also making a critical reading of this MS. The work would not have been possible without extensive computer resources provided over the years by Argonne's Mathematics and Computer Science Division (most recently on the IBM Blue Gene), Argonne's Laboratory Computing Resource Center, and the U.S. Department of Energy's National Energy Research Scientific Computing Center. This work is supported by the U.S. Department of Energy, Office of Nuclear Physics, under contract DE-AC02-06CH11357.

REFERENCES

- [1] BLATT J.M. A. K. M., *Phys. Rev.* , **91** (1953) 444.
- [2] CARLSON J. and SCHIAVILLA R., *Rev. Mod. Phys.* , **70** (1998) 743.
- [3] HAGEN G., DEAN D. J., HJORTH-JENSEN M., PAPENBROCK T. and SCHWENK A., *Phys. Rev. C* , **76** (2007) 044305.
- [4] WIRINGA R. B., STOKS V. G. J. and SCHIAVILLA R., *Phys. Rev. C* , **51** (1995) 38.
- [5] WIRINGA R. B., *Nucleon-nucleon interactions*, presented at *Contemporary Nuclear Shell Models*, edited by PAN X.-W., FENG D. H. and VALLIÈRES M. (Springer-Verlag, Berlin) 1997.
- [6] BERGERVOET J. R., VAN CAMPEN P. C., KLOMP R. A. M., DE KOK J.-L., RIJKEN T. A. and STOKS, V. G. J. AND. DE SWART J. J., *Phys. Rev. C* , **41** (1990) 1435.
- [7] STOKS V. G. J., KLOMP R. A. M. and RENTMEESTER, M. C. M. AND. DE SWART J. J., *Phys. Rev. C* , **48** (1993) 792.
- [8] PIEPER S. C., PANDHARIPANDE V. R., WIRINGA R. B. and CARLSON J., *Phys. Rev. C* , **64** (2001) 014001.
- [9] FUJITA J. and MIYAZAWA H., *Prog. Theor. Phys.* , **17** (1957) 360.
- [10] FUJITA J. and MIYAZAWA H., *Prog. Theor. Phys.* , **17** (1957) 366.
- [11] COON S. A. *et al.*, *Nucl. Phys. A*, **317** (1979) 242.
- [12] WIRINGA R. B. and PIEPER S., *Phys. Rev. Lett.* , **89** (2002) 182501.
- [13] PUDLINER B. S., PANDHARIPANDE V. R., CARLSON J., PIEPER S. C. and WIRINGA R. B., *Phys. Rev. C* , **56** (1997) 1720.
- [14] VOLKOV A. B., *Nucl. Phys A*, **74** (1965) 33.
- [15] CARLSON J. A. and WIRINGA R. B., *Variational monte-carlo techniques in nuclear physics*, in *Computational Nuclear Physics*, edited by LANGANKE K., MARUHN J. A. and KOONIN S. E., Vol. 1 (Springer-Verlag, Berlin) 1990, Ch. 9, the source and input files are available at http://www.phys.washington.edu/users/bulgac/Koonin/Monte_Carlo/.
- [16] PIEPER S. C., *Monte carlo calculations of nuclei*, in *Lecture Notes in Physics – Microscopic Quantum Many-Body Theories and Their Applications*, edited by NAVARRO J. and POLLS A., Vol. 510 (Springer-Verlag, Berlin) 1998.
- [17] PIEPER S. C. and WIRINGA R. B., *Ann. Rev. Nucl. Part. Sci.* , **51** (2001) 53.
- [18] WIRINGA R. B., *Phys. Rev. C* , **43** (1991) 1585.
- [19] WIRINGA R. B., PIEPER S. C., CARLSON J. and PANDHARIPANDE V. R., *Phys. Rev. C* , **62** (2000) 014001.
- [20] PIEPER S. C., VARGA K. and WIRINGA R. B., *Phys. Rev. C* , **66** (2002) 044310.
- [21] PIEPER S. C., WIRINGA R. B. and CARLSON J., *Phys. Rev. C* , **70** (2004) 054325.
- [22] SCHMIDT K. E. and LEE M. A., *Phys. Rev. E* , **51** (1995) 5495.
- [23] CEPERLEY D. M. and KALOS M. H., in *Monte Carlo Methods in Statistical Physics*, edited by BINDER K., Vol. 510 (Springer, Heidelberg) 1979.

- [24] NAVRÁTIL P. and ORMAND W. E., *Phys. Rev. C* , **68** (2003) 034305.
- [25] KURATH D., *Phys. Rev.* , **101** (1956) 216.
- [26] NOLEN J. A. and SCHIFFER J., *Ann. Rev. Nucl. Sci.* , **19** (1969) 471.
- [27] BARKER F. C., *Nucl.Phys.* , **83** (1966) 418.
- [28] WIRINGA R. B., PIEPER S. C. and PERVIN M., *Bull Am Phys Soc* , **52** (2007) 9, and in preparation.
- [29] MARQUÉS F. M. *et al.*, *Phys. Rev. C* , **65** (2002) 044006.
- [30] MARQUÉS F. M. and ORR N. A., *nucl-ex/03030005* , (2003) .
- [31] PIEPER S. C., *Phys. Rev. Lett.* , **90** (2003) 252501.
- [32] CARLSON J., *Nucl. Phys. A*, **522** (1991) 185c.
- [33] NOLLETT K., PIEPER S., WIRINGA R., CARLSON J. and HALE G. M., *Phys. Rev. Lett.* , **99** (2007) 022502.
- [34] HALE G. M., DODDER D. C. and WITTE K., *unpublished* , (1995) .
- [35] PUDLINER B. S., PANDHARIPANDE V. R., CARLSON J. and WIRINGA R. B., *Phys. Rev. Lett.* , **74** (1995) 4396.
- [36] WANG L.-B. *et al.*, *Phys. Rev. Lett.* , **93** (2003) 142501.
- [37] MUELLER P. *et al.*, *in preparation* , (2007) .
- [38] PIASETZKY E. and HIGINBOTHAM D., *private communication* , (2007) .
- [39] SCHIAVILLA R., WIRINGA R. B., PIEPER S. C. and CARLSON J., *Phys. Rev. Lett* , **98** (2007) 132501.
- [40] PERVIN M. and PIEPER, S. C. AND. WIRINGA R. B., *arXiv:0710.1265* , (2007) .
- [41] WUOSMAA A. H. *et al.*, *Phys. Rev. Lett.* , **94** (2005) 082502.
- [42] WUOSMAA A. H. *et al.*, *Phys. Rev. C* , **72** (2005) 061301(R).
- [43] FLAMBAUM V. V. and WIRINGA R. B., *Phys. Rev. C* , **76** (2007) , to be published, arXiv:0709.0077.